# Experimental Evidence of Edge Intrinsic Momentum Source Driven by Kinetic Ion Loss and Edge Radial Electric Fields in Tokamaks

J.A. Boedo<sup>1</sup>, J. S. deGrassie<sup>2</sup>, B. Grierson<sup>3</sup>, T. Stoltzfus-Dueck<sup>3</sup>, D. J. Battaglia<sup>3</sup>, D.L. Rudakov<sup>1</sup>, E.A. Belli<sup>2</sup>, R.J. Groebner,<sup>2</sup> E. Hollmann,<sup>1</sup> C. Lasnier<sup>4</sup>, W.M. Solomon,<sup>3</sup> E.A. Unterberg<sup>5</sup>, J. Watkins<sup>6</sup> and the DIII-D Team

<sup>1</sup>Center for Energy Research, University of California-San Diego, La Jolla, California 92093, USA

<sup>2</sup>General Atomics, PO Box 85608, San Diego, California 92186-5608, USA

<sup>3</sup>Princeton Plasma Physics Laboratory, Princeton, NJ 08543-0451, USA

<sup>4</sup>Lawrence Livermore National Laboratory, Livermore, California, 94551, USA

<sup>5</sup>Oak Ridge National Laboratory, Oak Ridge, Tennessee 37831, USA

<sup>6</sup>Sandia National Laboratories, Albuquerque, New Mexico 87185, USA

e-mail contact of main author: boedo@fusion.gat.com

(Received

#### **Abstract**

Bulk ion toroidal velocity profiles,  $V_{\parallel}^{D+}$ , peaking at 40-60 km/s are observed with Mach probes in a narrow edge region of DIII-D discharges without external momentum input. This intrinsic rotation can be well reproduced by a first principle, collisionless kinetic loss model of thermal ion loss that predicts the existence of a loss-cone distribution in velocity space resulting in a co-Ip directed velocity. We consider two kinetic models, one of which includes turbulence-enhanced momentum transport, as well as a third, the Pfirsch-Schluter (P-S) fluid mechanism. We measure a fine structure of the boundary radial electric field,  $E_{\rm r}$ , insofar ignored, featuring large (10–20 kV/m) positive peaks in the scrape off layer (SOL) at, or slightly inside, the last closed flux surface (LCFS) of these low power L- and H-mode discharges in DIII-D. The  $E_{\rm r}$  structure significantly affects the ion-loss model, extended to account for a non-uniform electric field. We also find that  $V_{\parallel}^{D+}$  is reduced when the magnetic topology is changed from lower single null (LSN) to upper single null (USN). The kinetic ion loss model

containing turbulence-enhanced momentum transport can explain the reduction, as we find that the potential fluctuations decay with radius, while we need to invoke a topology-enhanced collisionality on the simpler kinetic model. The P-S mechanism fails to reproduce the damping. We show a clear correlation between the near core  $V_{\parallel}^{C6+}$  velocity and the peak edge  $V_{\parallel}^{D+}$  in discharges with no external torque, further supporting the hypothesis that ion loss is the source for intrinsic torque in present tokamaks. However, we also show that when external torque is injected in the core, it can complete with, and eventually overwhelm, the edge source. Finally, we show some additional evidence that the ion/electron distribution in the SOL is non-Maxwellian.

PACS numbers: 52.55.Fa, 52.30.-q, 52.25.Fi

#### I. INTRODUCTION

Tokamak plasmas feature toroidal rotation without any external torque 1,23,4, <sup>5,6,7,8,9,10,11,12,13,14,15,16</sup>, called "intrinsic rotation". Initial observations were realized in balanced ICRH-heated<sup>3,5,6,7</sup> or NBI heated plasmas with perpendicular injection<sup>1</sup> and also observed in ohmically heated (OH) discharges as well<sup>1,4,7,14</sup>. Plasma rotation, and its shear, are of great importance 17,11 for tokamaks as they are critically involved in confinement, 18 plasma response to neoclassical tearing modes (NTM), 19,20 resistive wall modes,<sup>4</sup> and the threshold and dynamics of the transition from low confinement regimes (L-mode) to high confinement regimes<sup>21</sup> (H-mode), among other effects. The source of intrinsic rotation is thought to be located at the edge, <sup>11,12,13</sup> and attempts at producing a scaling with plasma parameters, 30,22,23, led to a prediction of a linear dependence on the edge/pedestal ion temperature  $V_{\parallel}^{D+} \propto T_i/I_p$  inside the LCFS and  $V_{\parallel}^{D+} \propto \sqrt{T_i}/I_p$  at the LCFS. If accompanied by an inward momentum pinch, discovered in JT-60U<sup>24</sup>, or inward diffusion, the edge intrinsic torque could spin the whole plasma<sup>25</sup>. Initial theoretical explanation for an inward pinch was given by Coppi<sup>26,27,28</sup> based on momentum convected by magnetosonic whistler-like nonlocal modes. Other mechanisms proposed for this edge intrinsic torque include thermal ion orbit loss<sup>29,30,31,32,33,34</sup>, turbulence-driven momentum<sup>35,</sup>  $^{36,37,38}$  such as Reynolds Stress $^{39, 40}$ , and conjectures involving influence from the scrape-off-layer (SOL) flows $^{41,42}$ . Early results of intrinsic plasma rotation in RF-heated plasmas $^{5,6}$  were explained by the excitation of two classes of intrinsic magnetosonic whistler-like modes $^{26,27}$ , one at the edge, containing momentum in the direction of the plasma current, and the other, non-local, convecting conter-current momentum out of the plasma. Intrinsic rotation can be critical for burning plasmas to increase stability and to transition into H-mode as the large moment of inertia in large plasmas makes it difficult to rotate them using only external torque. Additionally, the L-H power threshold,  $P_{thres}$ , in future devices can be large, about 70-80 MW for ITER $^{43}$  as estimated from the scaling law $^{44}$   $P_{Thres}$  = 2.15  $e^{\pm 0.107} n_{ne20}^{0.782} B_T^{0.772} a_{0.975}^{0.995} R^{0.999}$  that is roughly linear with density. There is a minimum in  $P_{thres}$  at low density and collisionality, where ITER would seek to operate, although if the density is lowered further  $P_{thres}$  increases due to an unknown mechanism thought to be turbulence-driven $^{45}$ . We will see that there is a collisionality/density dependence on the intrinsic rotation.

In this article we present D<sup>+</sup> parallel velocity measurements from Mach probes and C<sup>6+</sup> velocity measurements from charge exchange recombination (CER) spectroscopy and then compared the results to several theories, namely: 1) first-principle, colllisionless, kinetic computation of selective thermal ion loss due to a loss cone, 2) selective ion thermal loss enhanced by turbulence gradient and 3) Pfirsch-Schluter mechanism. We also show that near SOL flows follow the edge source and that kinetic and non-Maxwellian effects are significant in the edge and SOL of DIII-D discharges.

#### II. EXPERIMENTAL SETUP

Experiments where conducted in the DIII-D tokamak<sup>46</sup> on deuterium discharges in steady conditions Fig. 1 and where we scanned the collisionality by changing density (Fig. 1-a) and temperature. We created plasmas with no external momentum input (ohmic, and ECH-heated L-mode), or very low momentum input (low power NBI-heated L-modes and H-modes) with superimposed short ( $\sim 5$ -15 ms) neutral beam injection (NBI) blips for diagnostic purposes, as seen in Fig 1-e, to keep intrinsic rotation as the dominant mechanism (Fig. 1-f). Discharges in symmetrical upper single null (USN) and lower single null (LSN) shapes were used with the standard toroidal magnetic field ( $B_T$ ) configuration (clockwise from top), as seen in Fig. 2, resulting in the ion  $\nabla B$  drift directed to or away from the active divertor. Discharges had toroidal field,  $B_T = 1.7 - 2.0 \, \text{T}$ , major radius,  $R = 1.74 \, \text{m}$ , total (OH+auxiliary) discharge power range,  $P_{tot} \approx 1.5 - 4.5 MW$ , energy content range,  $W \approx 0.1 - 0.18 \, \text{MJ}$ , electron density,  $n_e \approx 0.8 - 6 \times 10^{13} \, cm^{-3}$ , and positive (counter-clockwise viewed from above) or negative plasma current,  $I_p = 1.0 \, \text{MA}$  as shown in Fig. 1

A fast scanning probe array<sup>27</sup> is introduced horizontally near the midplane (Fig. 2 inserts) to measure ion saturation current, electron temperature  $T_e$ , electron density  $n_e$ , floating potential  $\Phi_{\rm f}$  and the parallel plasma Mach number in the boundary. The probe is in the plasma for approximately 80 ms. We use magnetic reconstruction obtained from EFIT<sup>28</sup> to map the data in normalized flux coordinates.

The Mach tips, aligned along the parallel magnetic field, are usually voltage-swept at  $\sim 1 \, \text{kHz}$  to prevent sustained arcing and the signals are digitized at 5 MHz. We utilize well-known models by Chung and Hutchinson<sup>29-31</sup> to interpret the measured probe

currents as a Mach number and with a normalized viscosity<sup>31</sup>  $\alpha = 1$ . The plasma flow velocity is obtained by multiplying the local Mach number by the local sound speed  $C_s = \left[k(ZT_e + T_i)/m_i\right]^{1/2}$  assuming  $T_i = T_e$ , where k is the Boltzmann constant,  $T_e$  and  $T_i$  are the electron and ion temperature,  $T_e$  is the charge state and  $T_e$  is the ion mass. Flow is positive if flowing in the direction of the plasma current. The plasma potential  $V_{pl}$  is calculated from the floating potential  $\Phi_f$  and  $T_e$  as  $V_{pl} = \Phi_f + 2.5T_e$ , following the sheath theory for  $T_e$ . The CER diagnostic, described elsewhere, measures the ion temperature  $T_e$  and a core Thomson Scattering (TS) system<sup>47</sup> measures electron temperature and density

# III. RESULTS

In this section, we will show measurements of D<sup>+</sup> and C<sup>6+</sup> ion velocity profiles at the plasma edge under various conditions and compare them to kinetic and fluid theories to show that crucial features in the edge and SOL D+ velocity are due to kinetic effects.

The measured toroidal velocity profiles of D<sup>+</sup> and C<sup>6+</sup> ions in the plasma edge and SOL are shown in Fig. 3, diamonds from Mach probe, squares from Main Ion CER or miCER<sup>48,49</sup>, and circles for  $C^{6+}$  CER. The probes and miCER agree well although they are uncorrected for different spatial resolutions and integration volume, and is apparent that: 1)  $V_{\parallel}^{D+}$  features a peaked edge profile reaching speeds as high as 80 km/s, 2) the profile peaks at/near the LCFS<sup>50</sup> and 3)  $V_{\parallel}^{C6+}$  is not a proxy for  $V_{\parallel}^{D+}$  at the plasma edge, as previously reported<sup>50,51</sup>.

We observe a new feature, an up-down asymmetry in the midplane  $V_{\parallel}^{D+}$  profiles with

magnetic geometry. Probe-measured  $V_{\parallel}^{D+}$  profiles are shown in Fig. 4 for otherwise similar discharges in USN (dashed lines) and LSN (solid lines) magnetic configurations and for the plasma current in forward and also reversed direction. The data show, in addition to the features indicated above, that: 1) Edge  $V_{\parallel}^{D+}$  is always co-Ip and, 2) the  $V_{\parallel}^{D+}$  profile seems to be dampened throughout in USN geometry. We will discuss these results and compare to existing understanding of edge velocity generation; namely, two kinetic models based on thermal ion loss and the Pfirsch-Schluter fluid model. The ions in the DIII-D confined edge region are typically in the plateau regime, thus they can escape on a trajectory that is shorter then the mean-free path, justifying our use of the thermal ion loss models.

# III-1. THERMAL ION LOSS MODEL (KINETIC)

This collisionless mechanism<sup>29,30</sup> is based on the fact that ions within a region of about twice an ion poloidal gyroradius inside the LCFS can be lost due to a loss cone that favors removing the counter-Ip moving ions thus creating, when integrated over the resulting non-Maxwellian distribution function, a co-moving flow. The emergence of a loss cone for thermal ions in the edge was first identified by Chankin<sup>52</sup> but its relevance to edge flow was not realized until later, when Chang and Ku<sup>53</sup> pointed out a possible role of the loss cone on flow generation and, finally, deGrassie produced a basic physics model that quantified the velocity generation mechanism and followed existing scaling<sup>1</sup>, <sup>12</sup>, <sup>29</sup>.

We will follow work by deGrassie here, extended to include a non-uniform electric field, to compute  $V_{\parallel}^{D+}$  profiles numerically by launching an ensemble of particles with

various pitch angles and an energy distribution consistent with a given  $T_i$  profile and keeping track of the distribution function as *passing and trapped* particles drift in the magnetic field and exit into the SOL and eventually the plasma. Furthermore, deGrassie<sup>30</sup> shows that the computed ion velocity from the thermal ion loss model has a simple ion temperature scaling of  $V_{\parallel}^{D+} \approx T_i/I_p$  inside the LCFS and  $V_{\parallel}^{D+} \approx \sqrt{T_i}/I_p$  near the LCFS, and a dependence with magnetic mirror geometry, represented by the radii of the midplane,  $R_1$ , and X-point,  $R_x$ , (see Fig. 2) and radial electric field,  $E_r$ :

$$\begin{split} V_{\parallel} &= V_{th} \times \left\{ \frac{S_{x0}^2}{1 + c_{x0}} \sqrt{\frac{2}{\pi}} - \frac{S_{x0}^2 c_{x0}}{1 + c_{x0}} \tilde{\omega}_x \right\} \\ S_{x0}^2 &= R_x / R_1; \quad c_{x0} = \sqrt{1 - S_{x0}^2}; \quad \tilde{\omega}_x = -\left(1 + \sqrt{1 - S_{x0}^2}\right) \frac{E_r}{V_{th} B_{\theta}} \end{split}$$
 Eq. 1

which can be summarized as:

$$V_{\parallel} = a \left[ V_{th} + b \left( E_r / B_{\theta} \right) \right]; \quad a \left( R_x / R_1 \right), \quad b \left( R_x / R_1 \right)$$
 Eq. 2

In the loss cone model, a non-uniform electric field has the effects of: 1) shifting the velocity space boundaries between passing and trapped orbits and, 2) making the boundary energy-dependent, as previously demonstrated<sup>30</sup>. Notice that the dependence with  $T_i/I_p$  inside the LCFS is consistent with previous scaling laws<sup>29</sup> but the  $E_r$  dependence is a new result.

We show in Fig. 5 numerical computations of the  $V_{\parallel}^{D+}$  profiles as solid lines, where the measured non-uniform electric field,  $E_r$ , has been included for the first time, while the corresponding zero radial electric field computations are shown in dashed lines and the measurement of  $V_{\parallel}^{D+}$  from Mach probes, is shown as black dots. The cases considered are a) OH plasma with X-point radius, Rx, at 1.53 m, b) OH plasma with Rx

shifted by 10 cm to 1.63 m, and c) H-mode plasma with Rx=1.63 m. The loss cone calculations shown in Fig. 5 also include changes in the magnetic geometry (mirror ratio), or  $S_{x0}$ , which in the cases shown, was scanned by moving the X-point radius from  $R_x$ =1.53m (Fig. 5-a) to  $R_x$ =1.63m (Fig. 5-b-c) while maintaining the midplane radius  $R_1$  at 2.28m, as shown in Fig. 2(right). The magnitude of the change of the geometry factor,  $S_{x0}^2$  in these experiments is about 5% and variations between Fig. 5-a and Fig. 5-b are due to this change plus subtle variations in  $T_i$ . The deGrassie model produces a good fit in the SOL and across the LCFS, but the prediction is ineffective deeper into the core, as the fraction of lost particles vanishes and the model contains no momentum transport.

Note in Fig. 5 that the inclusion of  $E_r$  has the significant effect of: 1) increasing the peak velocity by 20-30%, 2) broadening the profiles by factors of 2 or more, and 3) introducing structure in the profiles that correlate to features in  $E_r$ , as shown next. It is also noticeable that the velocity peak can be higher in L-mode than in H-mode, a fact little noted in the past that suggests the feature is not driven by pressure gradients..

An important part of this work is related to the realization that  $E_r$  has a fine structure at the plasma edge and SOL that has been previously ignored. Profiles of high resolution (1.6 mm), probe-measured  $E_r = -\nabla_r V_{pl}$ , are shown in Fig. 6 for an H-mode (left) and L-mode discharges (right) as solid red lines, and compared to  $E_r$  obtained from the edge CER diagnostic (6 mm resolution) via the radial force balance,  $E_r = \left(Z_i e n_i\right)^{-1} \nabla P_i - v_{\theta i} B_{\phi i} + v_{\phi i} B_{\theta}$ , for  $C^{6+}$ , as solid circles and diamonds. Note that  $E_r$  reaches values of 10-20 kV/m in discrete peaks located at the LCFS and ~2 cm into the SOL, and there is good CER-probe data agreement throughout, particularly inside the

LCFS, with  $E_r$  featuring the characteristic H-mode deep well. There are no structures in the vacuum vessel to explain the peaks in the SOL and the physics driving the  $E_r$  field structure is as yet unknown.

The collisionless model of deGrassie, even including non-uniform  $E_r$ , does not reproduce the surprising result of Fig. 4, where otherwise similar discharges with either USN or LSN divertor geometry ( ion  $\nabla B$  drift down) feature drastically different  $V_{\parallel}^{D+}$  edge profiles. We show in Fig. 7 the calculations using deGrassie's model as blue (USN) and black (LSN) solid lines, and the probe measurements as blue squares (USN) and black circles (LSN). The calculated USN and LSN  $V_{\parallel}^{D+}$  profiles, obtained from the deGrassie's collisionless model, using the measured magnetic topology,  $T_i$  and  $E_r$  profiles, are not too different from each other, as expected from similar discharges whose only difference is an up-down  $\nabla B$  driven asymmetry. Furthermore, the calculated  $V_{\parallel}^{D+}$  profiles roughly match the LSN measurement but the discrepancy with the USN measurement is large, i.e. the deGrassie model cannot reproduce the USN measurement.

We advance the explanation, previously suggested by Shaing<sup>54</sup>, that the difference lies in trapped particle collisionality as the trapped particles have considerably larger trajectories when the  $\nabla B$  ion drift is away from the X-point and therefore the loss cone will tend to get refilled by scattered particles, reducing the distribution function asymmetry and thus, the resulting velocity. Calculations of the orbit length of trapped particles launched at the midplane for USN and LSN configurations were made with a particle-tracking code for Ti=200 eV and various pitch angles. Typical orbit tracing results, in red, are shown in Fig. 8 together with the corresponding particle path length,  $L_{\parallel}$ , and indicate a rough doubling of the trapped particle path length in USN compared to

LSN by a factor  $F \approx 5/3$ , in agreement with expectations. Therefore, the normalized ion collisionality  $^{55}$ , defined as  $v_i^* = 4.9 \times 10^{-18} \left(qRn_eZ_{eff} \ln \Lambda_i/T_i^2 \varepsilon^{3/2}\right)$ , which contains a measure of the orbit length as qR, should be corrected, for the trapped particles, as FqR. The normalized collisionality for the discharges considered in this paper is in the range  $0.7 \le v_i^* \le 5$ , while the corrected one is  $1.16 \le v_{i\_corr}^* \le 8.3$ . Collisionality is calculated at the edge using the near edge (R-Rsep~ -2—4 cm) TS and CER cords and assuming  $T_i^{C6+} = T_i^{D+}$ . Higher  $v_i^*$  values are for high density  $(3.5 \times 10^{13} \, \text{cm}^{-3})$ , low  $T_i$ , OH and ECH-heated discharges, and lower  $v_i^*$  values correspond to low-density  $(1.0 \times 10^{13} \, \text{cm}^{-3})$ , higher  $T_i$ , ECH-heated discharges. Thus trapped particles in USN configuration, at almost double the collisionality in LSN will tend to fill the loss cone in velocity space, thus reducing the effective plasma velocity.

We conclude that the deGrassie model including a realistic electric field predicts  $V_{\parallel}^{D+}$  profiles across the LCFS and into the SOL within a wide parameter range, so it seems to capture essential physics indicating kinetic effects are crucial to understand edge rotation/flows and also that trapped particle effects are relevant. This collissionless model fails to predict USN cases, over-predicting the measured velocity by a factor of 3, and since the USN-LSN discharges feature almost identical profiles, kinetic effects are again a very likely cause.

# III-2. THERMAL ION LOSS WITH TURBULENCE MODEL (KINETIC)

In this section, we will compare probe data to a kinetic model<sup>37,38</sup> by Stoltzfus-Dueck, also collisionless, which describes the physics of rotation generation by enhanced losses of counter *passing* ions (trapped not included) due to a turbulence field gradient. A key

element of this model is that the turbulence levels are higher further inside the plasma, decaying towards the SOL, and ballooning in character. Since co-current flowing ion orbits shift slightly outward and counter-current flowing ions orbits slightly inward, as illustrated in Fig. 9, the later are exposed to higher fluctuation levels (illustrated as dotted background) and thus diffuse radially faster due to turbulent  $E \times B$  drift resulting into more counter-current ion losses and a co-rotating bulk plasma. The model solves approximately an axisymmetric, collisionless, electrostatic drift-kinetic transport equation for the ions, following Hahm<sup>56</sup>.

An analytical expression can be obtained from the model at its simplest limit that predicts a flux-surfaced averaged deuterium rotation at the top of the pedestal, a region where the deGrassie model from Sec. III-1 predicts a small velocity.

$$V_{\phi_{-}pt}^{D+} \approx 0.104 \left(0.5d_{c} - \cos y_{0}\right) \frac{q}{L_{\phi}(cm)} \frac{T_{i}^{pt}(eV)}{B_{T}(T)} \quad km/s$$

where  $V_{\phi_-pt}^{D+}$  is the flux surface-averaged D+ rotation at the pedestal top (pt),  $d_c$  is an in-out transport asymmetry coefficient (~0.8-1.0),  $\cos y_0 = 2(R_X - R_0)/(R_{out} - R_{in})$  is a normalized X-point location, which is -1 for HFS X-point and +1 for LFS X-point,  $T_i^{pt}$  the ion temperature at the pedestal top and  $L_\phi$  is the e-folding decay length for the amplitude of potential fluctuations (high-pass filtered to avoid GAMs). Notice the velocity is proportional to  $T_i/I_p$  following existing scaling laws<sup>30</sup>. When measured parameters are used, we obtain 37 km/s, comparable to the measured value.

To obtain a more accurate solution, the equation:

$$\partial_t f_i + b_{\phi} \upsilon \partial_{\nu} f_i - b_{\phi} \delta \upsilon^2 (\sin y) \partial_x f_i - D(y) \partial_x (e^{-x} \partial_x f_i) = 0$$

for the axisymmetric parallel ion distribution function,  $f_i(x,y,\upsilon,t)$  is solved, following Refs. 19-20, in a radially thin, magnetic geometry where x is the radial position, y the poloidal position, with the confined plasma at  $x \le 0$  and SOL at x>0. The parallel velocity is  $\upsilon$ , magnetic field  $B = \left(B_\theta b_\theta \hat{\theta} + B_\phi b_\phi \hat{\phi}\right) \left(R_0/R\right)$ , the dimensionless parameter  $\delta = q \rho_{ilpt}/L_\phi$  that contains the curvature drift, ion thermal gyroradius  $\rho_i = \upsilon_{ii}/\Omega_i$ , safety factor  $q = aB_\phi/R_0 B_\theta$ , radial diffusivity D(y) and potential fluctuation decay length  $L_\phi$ . Measured experimental profiles and parameters are used as input to the model, and  $d_c$  is set to a strong ballooning regime (~1.0) and the velocity profile is the integral of the distribution at various radii.

The calculated  $V_{\parallel}^{D+}$  profiles are shown in Fig. 10-a as solid lines for USN (grey) and LSN (black), where key features are that: 1) the  $V_{\parallel}^{D+}$  peak at/near the LCFS is reproduced in magnitude, and 2) the much lower  $V_{\parallel}^{D+}$  velocity in USN geometry is also reproduced. The measured  $V_{\parallel}^{D+}$  profiles for USN (grey circles) and LSN (black circles) are overlayed in Fig. 10-a for comparison.

The measured profiles of  $\tilde{V}_{pl}$  and  $\tilde{E}_{\theta}$ , high-pass filtered above 15 kHz to avoid the contribution of GAMs, and evaluated as rms levels, are shown in Figs. 10-b-c, and two features are clear: 1)  $\tilde{V}_{pl}$  and  $\tilde{E}_{\theta}$  rms levels decay monotonically with radius with a significant gradient, a key element of the model, and 2) the fluctuation levels change significantly inside the LCFS with USN/LSN magnetic geometry, a new result.

To summarize, the Stoltzfus-Dueck model, which depends on a potential turbulence gradient to transport momentum of passing counter-Ip particles outward, can explain both the  $V_{\parallel}^{D+}$  profile magnitude and shape and the observed reduction in  $V_{\parallel}^{D+}$  with LSN to USN geometry change. We also observe experimentally the radially-decaying turbulence intensity profile needed by the model.

# III-3. FLUID FORMULATION, PFIRSCH-SCHLUTER MODEL

In this section we will compare probe-measured velocity profiles to calculations using the Pfirsch-Schluter mechanism, initially pointed-out by Hugill<sup>57</sup>, resulting from the fact that the two main fluid drifts, the ExB and diamagnetic, are not divergence-free, thus driving parallel mass flow. The original expression for the expected parallel velocity  $V_{\parallel}^{PS}$  by Hugill:

$$V_{\parallel}^{PS} = 2q\cos(\theta) \left(\frac{E_r}{B} - \frac{\nabla P_i}{enB}\right)$$

contains a clear dependence on the radial electric field  $E_r$ , ion pressure gradient  $\nabla P_i$ , and poloidal location,  $\theta$ . The expression has been improved by Chankin<sup>58</sup> by properly accounting for the "return flow"  $E_r/B_\theta$ , obtaining:

$$V_{\parallel}^{PS} = \frac{E_r}{B_{\theta}} - 2\frac{a}{R}\frac{B}{B_{\theta}}\frac{\nabla P_i}{enB} \left(1 + \frac{\tan^2(\theta)}{k^2}\right)^{-1/2}$$

which, at the outer/inner midplane, is reduced to

$$V_{\parallel}^{iPS} = \frac{E_r}{B_{\theta}} \pm 2 \frac{a}{R} \frac{B}{B_{\theta}} \frac{\nabla P_i}{enB}, \quad \alpha = 0, \pi$$

For purposes of further comparison using various diagnostics, we will name the two terms as:

$$PS_1 = \frac{E_r}{B_\theta}$$
 and  $PS_2 = 2\frac{a}{R}\frac{B}{B_\theta}\frac{\nabla P_i}{enB}$ ,  $\alpha = 0$ 

The P-S terms are often calculated in the literature using only probe data  $^{42}$ ,  $^{58}$ ,  $^{50}$ ,  $^{60}$ , and therefore the second (PS<sub>2</sub>) gradient term is calculated assuming  $\nabla P_i = \nabla P_e$  (by taking  $n_i = n_e$  and  $T_i^{D+} = T_e$ , as  $T_i^{D+}$  or  $T_i^{C6+}$  measurements are not often available at the SOL/edge of tokamaks). In this paper, the second term, PS<sub>2</sub>, will be evaluated independently by: 1) using probe data, 2) TS data (i.e. assuming  $T_i^{D+} = T_e$  as is customary), and, 3) by using  $T_i^{C6+}$  data from CER. The use of  $T_i^{C6+}$  is a considerable improvement upon the existing device dataset as it allows a more realistic evaluation of  $\nabla P_i$  across the LCFS although we still use some assumptions such as  $n_e = n_i$ ,  $T_i^{C6+} = T_i^{D+}$  and  $T_i^{\parallel} = T_i^{\perp}$ . We will compare the terms calculated from the various datasets to each other and to the probe-measured parallel velocity.

As the P-S calculation depends on gradients (of both  $P_i$  and  $V_{pl}$ ), reproducibility is an issue, so we first compare both profiles and P-S calculations from two identical discharges using probe (for both the PS<sub>1</sub> and PS<sub>2</sub> terms), as seen in Fig. 11-a to benchmark how much discharge-to discharge scatter is obtained. We have overlaid measured profiles of  $T_e$  (squares from TS, diamonds from probe),  $T_i$  (circles) in Fig. 11-c, and of  $n_e$  (circles from TS, diamonds from Probe) in Fig. 11-b for both discharges. The polynomial fits to the TS and CER data are shown as lines (solid and dashed) in Figs 11-b-c. Several relevant observations come immediately to mind: 1)  $T_i^{C6+} > T_e$  in the edge and SOL which is surprising in ECH-heated discharges, 2)  $\nabla T_i^{C6+}$  is clearly much larger than  $\nabla T_e$  in the near SOL, 3)  $T_e$  and  $n_e$  data from TS and probes overlap well across the LCFS and into the core and, 4) the TS and CER  $T_e$ ,  $n_e$  and  $T_i^{C6+}$  data and their

polynomial fits seem fairly reproducible for the two identical discharges. We compare the calculated P-S components (PS<sub>1</sub>, PS<sub>2</sub> and the total, PS<sub>i</sub>) derived solely from probe data (thus assuming  $T_e = T_i$ ,  $n_e = n_i$ ) on Fig. 11-a to assess reproducibility and sensitivity on  $E_r$  and  $\nabla P$ . We find that: 1) the variability of the full term, PS<sub>t</sub> (dark lines) is roughly 30% at the LCFS and near SOL, increasing to about 90% in the far SOL, 2) the P-S calculations compare to Mach probe velocity measurements (light lines) within 20% at the LCFS and near SOL and increase to as much as 50% in the far SOL and, 3) the PS<sub>1</sub> term (solid symbols) tends to be 50% smaller than the PS<sub>2</sub> term (open symbols). In short, agreement at the LCFS and in the first 2 cm of the SOL (assuming  $T_e = T_i$ ,  $n_e = n_i$ ) is within 30% between calculations and measurements, worse further out.

A more accurate comparison between Mach probe data and the P-S model can be made by using the polynomial-fitted  $T_i^{C6+}$  from CER assuming  $T_i^{D+} = T_i^{C6+}$  to calculate  $\nabla P_i \approx \nabla \left(T_i^{C6+}n_e\right)$  in the diamagnetic term, PS<sub>2</sub>, and shown in Fig. 12 as a thick gray line labeled " $PS_2^i$  CER". The same term is computed, for comparison, using the polynomial-fitted  $T_e$ ,  $n_e$  from TS, and the assumption  $\nabla P_i \approx \nabla P_e = \nabla \left(T_e n_e\right)$  shown as a dashed thick dashed gray line labeled " $PS_2^e$  TS", and, independently using  $T_e$ ,  $n_e$  from probes, shown as a thick dashed black line with circles labeled " $PS_2^e$  Pr obe". We also calculate the total P-S flow from probe data, shown as thick dashed black line labeled " $PS_i$  Pr obe". The electric field term,  $P_{s1}$ , calculated from probe data is shown as filled circles. Finally, the measured flow from Mach probes is shown as large hexagons.

We find that all PS2 calculations are in reasonable agreement near the LCFS but

diverge markedly into the SOL, and we find surprising that the use of  $T_i^{C6+}$  in the  $\nabla P_i$  calculation causes it to markedly diverge from the measurements. The calculation that uses CER  $T_i^{C6+}$  and TS  $n_e$  ( $PS_2^i$ , solid light line) to calculate  $\nabla P_i$  grows quickly into the SOL due to the increasing  $T_i^{C6+}$  gradient, as seen in Fig. 11-c, whereas the calculation using TS  $T_e$  and  $n_e$  ( $PS_2^e$ , dashed light line) vanishes into the SOL, dominated by the flattening  $T_e$  profile. Calculations of P-S using the PS<sub>2</sub> from TS or CER data would grossly under-predict or over-predict the  $V_{\parallel}^{D+}$  probe measurements in the SOL respectively. Finally, we use high spatial resolution  $T_e$  and  $n_e$  from the probe system to calculate  $PS_2^e$ -probe (dashed dark line with circles), which is overlaid in Fig. 12, and agrees with the other calculations near the LCFS. We show, for completeness, the  $E_r$  based term ( $PS_1$ , solid circles) and the full P-S calculation based on probe data,  $PS_i$ -probe (solid black line), and also the measured  $V_{\parallel}^{D+}$  profile (solid hexaedrons).

In summary, we find that: 1) PS<sub>2</sub> from TS, CER and probe agree relatively well at and inside the LCFS but then diverge in the SOL, 2) PS<sub>2</sub> from probe and TS data has a wider region of agreement around the LCFS, and 3) the full P-S calculation,  $PS_t$  – probe agrees well with the actual  $V_{\parallel}^{D+}$  probe measurement around the LCFS, but over-predicts it in the SOL by about 30%.

The result that using  $\nabla P = \nabla \left(T_i^{C6+} n_e\right)$  leads to an overall lesser agreement compared to the measurement across the SOL is puzzling but then the P-S flows are a fluid effect and thus the Chankin P-S derivation (and all others) assumes Maxwellian distributions, no significant sources or sinks of particles in the SOL, and does not account for other

sources of flow. It is known that these assumptions are violated in the SOL in these discharges. It is also likely, as long predicted by kinetic simulations and ratified by recent, state of the art kinetic calculations<sup>62</sup>, that  $T_i^{C6+} \neq T_i^{D+}$  and that  $T_i^{\parallel} \neq T_i^{\perp}$ , i.e. the distribution function is not isotropic (and not Maxwellian) and that impurity and main population ions are not thermalized, effects that would become more pronounced at lower densities or in the SOL, consistent with what we see.

An indirect test of kinetic effects can be made by comparing similar USN and LSN discharges (Fig. 2-left) that seem to show either trapped particle collisionality effects or turbulence effects on passing particles, both distorting the bulk distribution function. The calculated P-S flow using probe data, with the assumptions described earlier, is shown in Fig. 13 for otherwise similar USN (light dashed line) and LSN (dark dashed line), and compared to the probe-measured velocity (light line-circles for USN and dark line-circles for LSN). It is quite clear that although  $V_{\parallel}^{D+}$  is almost fully dampened in the USN case, the predicted P-S flow is not, so the P-S fluid model fails in the USN case.

We conclude from this section that we can calculate velocity profiles for two identical discharges using the P-S model and obtain results with a variability, mostly from gradient calculations, of 20-30% near the LCFS and 70% in the far SOL. The P-S calculations compare to measured profiles within 20% at the LCFS and 50% at the far SOL and the diamagnetic term is dominant by far. If we improve upon historical P-S calculations by using  $\nabla P = \nabla \left(T_i^{C6+} n_e\right)$  instead of the customary approximation  $\nabla P \approx \nabla P_e = \nabla \left(T_e n_e\right)$  we find reasonable (20-30%) agreement with the  $V_{\parallel}^{D+}$  measurement at the LCFS and a strong divergence in the SOL due to the drop in  $T_i^{C6+}$  with radius. In short, aside from

agreement at the LCFS, the best P-S calculation we can make is not that close to the measurements in the SOL, a fact not surprising considering the constraints and assumptions generally made on deriving the model (such as absence of sources or sinks, up-down velocity condition, etc). We find strong evidence that kinetic effects need to be considered by the failure of the P-S model to reproduce the clearly observed USN-LSN asymmetry.

# IV. RELATION TO CORE AND SOL FLOWS

This section addresses a key question of this work, i.e. if the momentum contained in the flowing plasma layer near the LCFS is carried inward into the core or outward into the SOL by any mechanism and if this intrinsic layer is dominant or can be overwhelmed by other sources of momentum, such as neutral beam injection.

We performed experiments where 1.7 MW of either co or counter (i.e. injection in the direction of Ip or opposite) NBI injection was applied using de-rated beams in LSN discharges with density varying by  $1.8-3.5\times10^{13}$  cm<sup>-3</sup>. The beams apply a torque of about 1 N-m/MW. The CER-measured  $V_t^{C6+}$  profiles are shown in Fig. 14-a for co-NBI injection (solid lines) and counter-NBI injection (dashed lines) cases with density of  $1.9\times10^{13}$  cm<sup>-3</sup> (dark lines) and  $3.0\times10^{13}$  cm<sup>-3</sup> (gray lines). The probe-measured  $V_{\parallel}^{D+}$  profiles, shown in Fig. 14-b with the same line/color convention, reflect edge plasma velocity/flow in the SOL and across the LCFS.

It is clear in Fig. 14-a that the core  $V_t^{C6+}$  is reversed when counter-NBI injection is used (dashed lines), as expected, but it is notable that the edge  $V_t^{C6+}$  stays positive for all but the counter-NBI case at high  $(3.0 \times 10^{13} \text{ cm}^{-3})$  density, a consistently observed

behavior. The edge  $V_{\parallel}^{D+}$  profiles, shown in Fig. 14-b, stay positive in all cases but the velocity clearly drops to near-zero for the highest density  $(3.0 \times 10^{13} \text{ cm}^{-3})$  counter-NBI case. Previous work has shown<sup>50</sup> that the co and counter-NBI discharges have identical profiles and that a simple momentum balance evaluates the intrinsic momentum edge source at 0.31 N-m and the toroidal momentum diffusivity at  $\chi_{\phi} = 0.8 \, m^2/s$ . As the source of external torque at the core (NBI) clearly changes the LCFS/SOL velocity profile, we can then conclude that momentum injected in the core can diffuse into the LCFS/SOL and overwhelm the intrinsic momentum source, i.e. in NBI-heated tokamaks the near edge flow can be core-determined.

The effect of collisionality, with no external momentum input, on the core and SOL velocity profiles was studied in USN discharges using density and temperature scans. For a density scan in OH discharges, the measured core profiles are shown in Fig. 15-a and the edge profiles are shown in Fig. 15-b with matching lines and symbols. The core  $V_t^{C6+}$  profiles show a clear dependence on density, where at low density the profile is almost flat but it hollows out at medium density and flattens to zero at high density. The edge  $V_{\parallel}^{D+}$  profiles are roughly comparable for the low and medium density cases and their peak value roughly reflects the  $T_i^{C6+}$  temperature (CER-measured at ~4 cm inside the LCFS); however,  $V_{\parallel}^{D+}$  drops to zero for the highest density case as the collisionality increases by a factor of ~3,  $0.4 < v_i^* < 1.6$ , although we must remember that trapped particles in these USN discharges have an enhanced collisionality of  $0.8 < v_{i\_corr}^* < 3.2$ . We can argue that the edge intrinsic source has collapsed due to the increasing trapped particle collisionality at high density (enhanced by the USN geometry) and that the core

follows; however, the mid-density hollow profile is similar of that observed in various devices <sup>63</sup>, <sup>64</sup>, <sup>65</sup> and recently explained as an effect of non-Maxwellian equilibrium in turbulent momentum transport <sup>66</sup> when the collisionality regime transitions from banana to plateau, so a simple and straightforward explanation is not available yet.

If we repeat the density scan in USN discharges with ECH heating (no external momentum input), the core  $V_t^{C6+}$  profiles still show a strong dependence on density, as seen in Fig.16-a, while the edge  $V_{\parallel}^{D+}$  profiles, Fig. 16-b, have a weaker response. The results shown in Fig. 16 seem consistent with a persistent edge source resisting the effect of collisionality on core hollowing.

The discussion above suggests that phenomena other than an edge source with some inward momentum transport play a role in determining the edge velocity profile at densities above  $\sim 2.0\text{-}2.5 \times 10^{13}$  cm<sup>-3</sup> for these discharge types, most probably the non-Maxwellian mechanism unveiled by Barnes<sup>66</sup>. However, if we compare the edge  $V_{\parallel}^{D+}$  evaluated at/inside the LCFS with  $V_t^{C6+}$  evaluated at  $\psi = 0.8$  (or  $\sim 8$  cm towards the core), shown in Fig. 17, we obtain an reasonable correlation between edge deuteron velocity and the near-core plasma velocity which is consistent with the rotation source being at the plasma edge.

# V. ADDITIONAL EVIDENCE FOR NON-MAXWELLIAN DISTRIBUTIONS IN THE SOL

The measurement of ion saturation current,  $I_{sat}$ , obtained by measuring the current to a Langmuir probe when a sufficiently large (>3kT<sub>e</sub>) negative bias is applied to it, has

been long considered as a proxy for ion flux. However  $I_{sat}$  can also be estimated with information (i.e.  $T_e$ ) obtained far from saturation due to the fact that the probe characteristic is a well-known function  $^{67,68}$ . For example, expanding the probe characteristic in terms of zero-order Bessel functions  $^{69}$ ,  $I_{m\omega}$ , as function of the applied AC voltage's amplitude,  $U_0$ , frequency,  $\omega$ , and plasma temperature,  $T_e$ , gives:

$$I = 2\sum_{m=1}^{\infty} I_{m\omega} \cos(m\omega t); \quad I_{m\omega} = I_{sat} \frac{I_m (eU_0/kT_e)}{I_0 (eU_0/kT_e)}$$

This "harmonics technique" is often used to measure  $T_e$  with high time resolution <sup>69,70</sup>, when the probe tip is DC floating and the applied AC voltage is kept low ( $< kT_e$ ), thus operating at the floating potential, where the total current is zero, so the ion and electron currents are equal. If a given harmonic, such as the first or second one,  $I_{\omega}$ ,  $I_{2\omega}$ , are extracted from the probe total current (by FFT, filtering, or some other method), then one can obtain an "estimated"  $I_{sat}^{Est}$ , if  $U_0$ ,  $\omega$  and  $T_e$  are known:

$$I_{sat}^{Est} = (I_0 I_{2\omega})/2I_2$$

We now postulate that the ratio of the directly measured (by constant DC bias at V>  $3T_e$ ) to the estimated  $I_{sat}$ ,  $I_{sat}^{Meas}/I_{sat}^{Est}$  will be a measure of a departure from the Maxwellian distribution since  $I_{sat}^{Meas}$  should reflect any high electron or ion energy tail or any departure from Maxwellian, while  $I_{sat}^{Est}$  is computed assuming  $T_e$  from a Maxwellian distribution.

Profiles of the  $I_{sat}^{Meas}/I_{sat}^{Est}$  ratio for several discharges where the average density was varied between  $1.1 \times 10^{13} \, cm^{-3} \le n_e \le 3.3 \times 10^{13} \, cm^{-3}$  are shown in Fig. 18. The normalized ion and electron edge collisionality (measured ~2-3 cm inside the LCFS) varies strongly  $0.4 < v_i^* < 10$  and  $10 < v_e^* < 60$ , over the density, and concomitant temperature range of this data set. The  $I_{sat}^{Meas}/I_{sat}^{Est}$  ratio is ~1 inside the LCFS and rises as high as 4-5 across the SOL for all traces, labeled with the corresponding average density. There are two facts that support out earlier postulate: 1)  $I_{sat}^{Meas}/I_{sat}^{Est}$  increases in radius across the SOL as collisionality drops, and 2) the peak  $I_{sat}^{Meas}/I_{sat}^{Est}$  value tends towards a ratio of 1 with increasing density/collisionality. Both trends are expected if collisions tend to thermalize the plasma, dampen high energy tails and fill loss-cone originated gaps in the distribution function. We conclude that there is additional evidence supporting the existence of non-Maxwelian distributions and kinetic effects in the SOL.

#### VI. ITER ESTIMATE FROM ION LOSS

We used the ion loss model by deGrassie and profiles from ITER simulations produced by the ASTRA code<sup>71</sup>,<sup>72</sup> to estimate the intrinsic rotation expected for those plasmas. We considered several scenarios: 1) L-mode case with 33.5 MW of auxiliary heating, below the L-H threshold of 36 MW, 2) H-mode case with 50 MW of auxiliary heating and 3) and arbitrary case similar to case 2 with  $T_i^{C6+} \sim 10 - 20 \times T_e$  at the LCFS, based on DIII-D measured profiles for OH and ECH-heated discharges showing flat profiles at the edge with  $T_i^{C6+} >> T_e$ . Case 1 (not shown) yielded very low rotation due to low  $T_i$ , whereas cases 2 and 3, shown in Fig. 19, produce intrinsic  $V_{\parallel}^{D+}$  of  $\sim$ 40 km/s and 120 km/s,

respectively. Notice the extremely narrow ( $\sim$ 4-5mm) rotation layer, due to the high plasma current,  $I_p = 15MA$ , that reduces the trapped orbit radial extent. Some kind of transport mechanism would be required to transmit this momentum to the core.

#### VI. SUMMARY AND CONCLUSIONS

Ion thermal loss mechanisms can explain the measured edge  $\mathrm{D}^{\scriptscriptstyle{+}}$  parallel velocity,  $V_{\scriptscriptstyle \parallel}^{^{D+}}$  , profiles to a great degree in low collisionality conditions, while the Pfirsch-Schluter mechanism agrees at/near the LCFS but seems to fail in the SOL, probably due to non-Maxwellian features and source and sink terms that are neglected in this fluid model. The USN/LSN asymmetry found in  $V_{\parallel}^{D+}$  profiles can not be explained by Pfirsch-Schluter, nor by the deGrassie collisionless model unless we invoke an increased effective collisionality in USN. However, the USN/LSN asymmetry can be explained by the Stoltzfus-Dueck model, which includes enhanced passing particle momentum transport due to a turbulence gradient, which is different in USN and LSN. The turbulence intensity profile is also shown to be vanishing with increasing radius, a key element of the theory. Thus, we can conclude that kinetic models seem to capture the key physics involved in setting edge/SOL  $V_{\parallel}^{D+}$  profile, and that kinetic effects, involving passing and trapped particles, are important in establishing the edge and SOL velocity. We have also produced additional evidence of the existence of non-Maxwellian distribution function in the SOL and of the existence of electric field structure in the edge/SOL that strongly affects the loss cone mechanism.

We have also shown that in discharges with externally injected torque, edge/near SOL flows are affected by outward momentum transport from the core, tending to overwhelm the boundary mechanism, despite its resiliency, at large enough injected

torque. Additionally we show that the edge  $V_{\parallel}^{D+}$  velocity and the near-edge  $V_{\phi}^{C6+}$  core velocity are well-correlated (unless other core kinetic effects are dominant) supporting the edge source as the origin of intrinsic rotation in tokamaks.

# **ACKNOWLEDGMENTS**

This work was supported by the U.S. Department of Energy under DE-FG02-07ER54917, DE-AC02-09CH11466, DE-FG02-95ER54309, DE-FC02-04ER54698, DE-AC04-94AL85000, DE-AC52-07NA27344, and DE-AC05-00OR22725. The contribution of A. Polevoi and R. Pitts with ITER calculations is gratefully acknowledged. The technical contributions of L. Chousal, R. Hernandez are gratefully acknowledged. DIII-D data shown in this paper can be obtained in digital format by following the links at https://fusion.gat.com/global/D3D\_DMP.

# **List of Figure Captions**

- **Fig. 1**. Time volution of a discharge showing the OH and ECH+OH phases in shaded boxes in d). Probe data was taken at the times marked by vertical dashed lines. Neutral beam blips are seen in e) and corresponding CER measurements of TiC6+ and Vtor shown in f) and g).
- **Fig. 2.** EFIT magnetic reconstructions showing (left) symmetric upper and lower single null configurations and diagnostic locations (scanning probes, Thomson Scattering and CER) and, (right) X point scan configurations indicating midplane and X-point radial locations ( $R_1$  and  $R_2$  respectively).
- **Fig. 3.** Edge profiles of: scanning probe  $V_{\parallel}^{D+}$  (diamonds), main ion CER V $\phi$  (squares), and  $C^{6+}$  CER V $\phi$  (circles)
- **Fig. 4.** Probe-measured  $V_{\parallel}^{D+}$  edge profiles for LSN (solid lines) and USN (dashed lines) follow the sign of Ip. Clear dampening of the velocity is seen for the USN configuration.  $\nabla B$  points to the LSN divertor.
- **Fig. 5.**  $V_{\parallel}^{D+}$  profiles for OH (a-b) and H-mode (c) are calculated for  $E_r$ =0 (dashed) and using measured  $E_r$  (solid) and compared to that measured by a Mach probe (solid circles).
- **Fig. 6**. Comparison of radial electric field measured with probes (solid red line & symbols) and CER (solid symbols) for H-mode (left) and L-mode (right) discharges.
- **Fig. 7.**  $V_{\parallel}^{D+}$  measurements from probes for USN (squares) and LSN (circles) compared to loss cone calculations (blue and black solid lines respectively)
- **Fig. 8**. Parallel connection length comparison for trapped orbits (thick line) with two pitch angles in USN and LSN configurations.
- Fig. 9. Co- (red) and counter-Ip (blue) passing ion orbits in a background of ballooning

turbulence with a negative gradient (dot density).

**Fig. 10**. Comparison of USN (gray) and LSN (black) profiles of a)  $V_{\parallel}^{D+}$  profiles calculated from the S-D model , b) plasma potential Vpl and c)  $E_{\theta}^{rms}$ .

Fig. 11. Profiles for two identical discharges (open and solid symbols) of a) the predicted Pfirsch-Schluter  $V_{\parallel}^{D+}$  from probes (solid and dotted black lines) and its PS1 and PS2 components shown in symbols and compared to  $V_{\parallel}^{D+}$  data from a Mach probe, b)  $n_e$  from TS and probes with corresponding polynomial fits and c) electron  $T_e$  from TS and probes,  $T_i^{C6+}$  from CER and corresponding polynomial fits.

**Fig. 12.** Comparison of measured  $V_{\parallel}^{D+}$  data (large black hexagons) and P-S diamagnetic component calculated from TS data (dashed light line), from probe data (circles and solid dark line) and using Ti from CER data (solid light line). The Er component, (probemeasured) is show in solid circles and the full P-S (also probe measured), is shown in open circles.

**Fig. 13**. Comparison of measured  $V_{\parallel}^{D+}$  data (symbols) and P-S velocity calculated from probe data (dashed lines) for LSN (dark lines) and USN (light lines) configurations.

**Fig. 14**. Core  $V_{\varphi}^{C6+}$  profiles (left) for co-NBI (solid traces) and counter-NBI (dashed traces) phase of discharges with low  $(1.9 \times 10^{13}, \text{dark lines})$  and high  $(3.0 \times 10^{13}, \text{light line})$ s density. Probe-measured  $V_{\parallel}^{D+}$  edge profiles (right).

**Fig. 15.** a) Core  $V_{\varphi}^{C6+}$  profiles for OH phase of discharges with low  $(1.8 \times 10^{13} \text{ cm}^{-3} \text{ dark} \text{ line})$ , medium  $(2.3 \times 10^{13} \text{ cm}^{-3} \text{ dark} \text{ dashed line})$  and high  $(2.8 \times 10^{13} \text{ cm}^{-3} \text{ light line})$  density. b) Probe-measured  $V_{\parallel}^{D+}$  edge profiles.

- **Fig. 16.** a) Core  $V_{\varphi}^{C6+}$  profiles (left) for ECH phase of discharges with low (1.8x10<sup>13</sup> cm<sup>-3</sup> dark line), medium (2.3x10<sup>13</sup> cm<sup>-3</sup> dark dashed line) and high (2.8x10<sup>13</sup> cm<sup>-3</sup> light line) density. b) Probe-measured  $V_{\parallel}^{D+}$  edge profiles .
- **Fig. 17.** A near linear relationship exists between  $V_{\parallel}^{C6+}$  at Psi=0.8 and  $V_{\parallel}^{D+}$  at the LCFS for OH (open circles) and ECH (solid circles) discharges.
- **Fig. 18**. The ratio of measured Isat,  $I_{sat}^{Meas}$ , to estimated Isat,  $I_{sat}^{Est}$ , is unity in the core and increases in the SOL. The increase is more pronounced as density (indicated in units of  $x 10^{13}$  cm<sup>-3</sup>) drops. Density is a proxy for collisionality in these ECH-heated discharges.
- **Fig. 19.** Calculations of expected ITER rotation due to loss cone physics (top) for two Ti profile cases (bottom), one (dashed line) obtained by the ASTRA code and the other case (solid line) is an arbitrary profile that follows existing DIII-D experience with Ti> Te.

# **List of Figures**

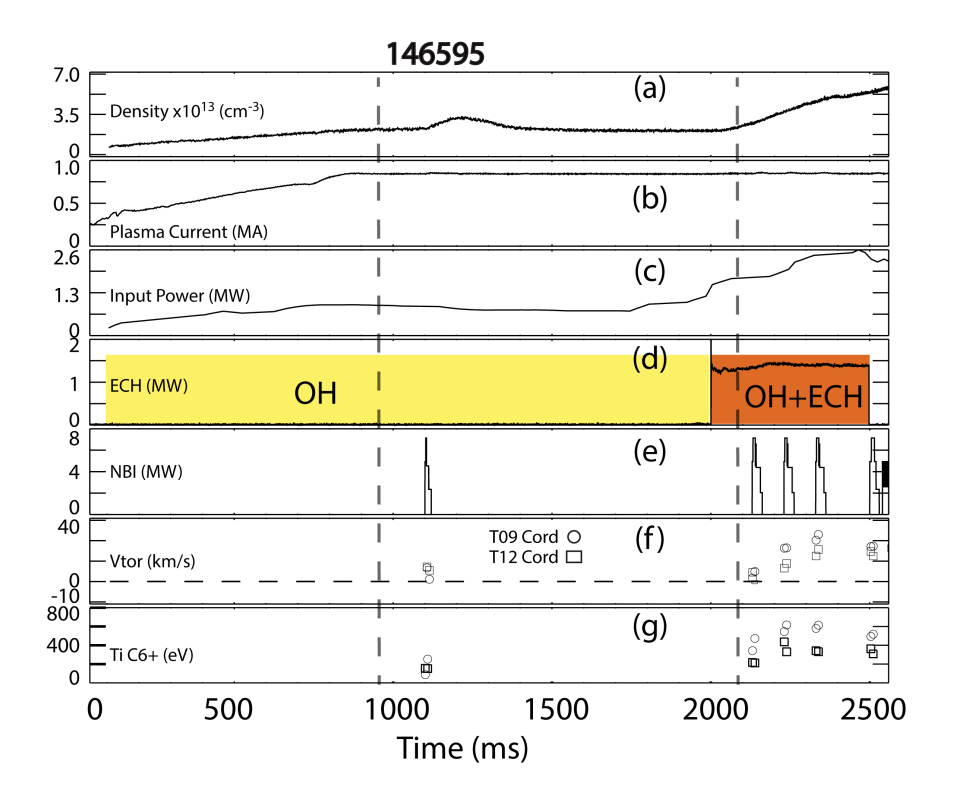


Fig. 1

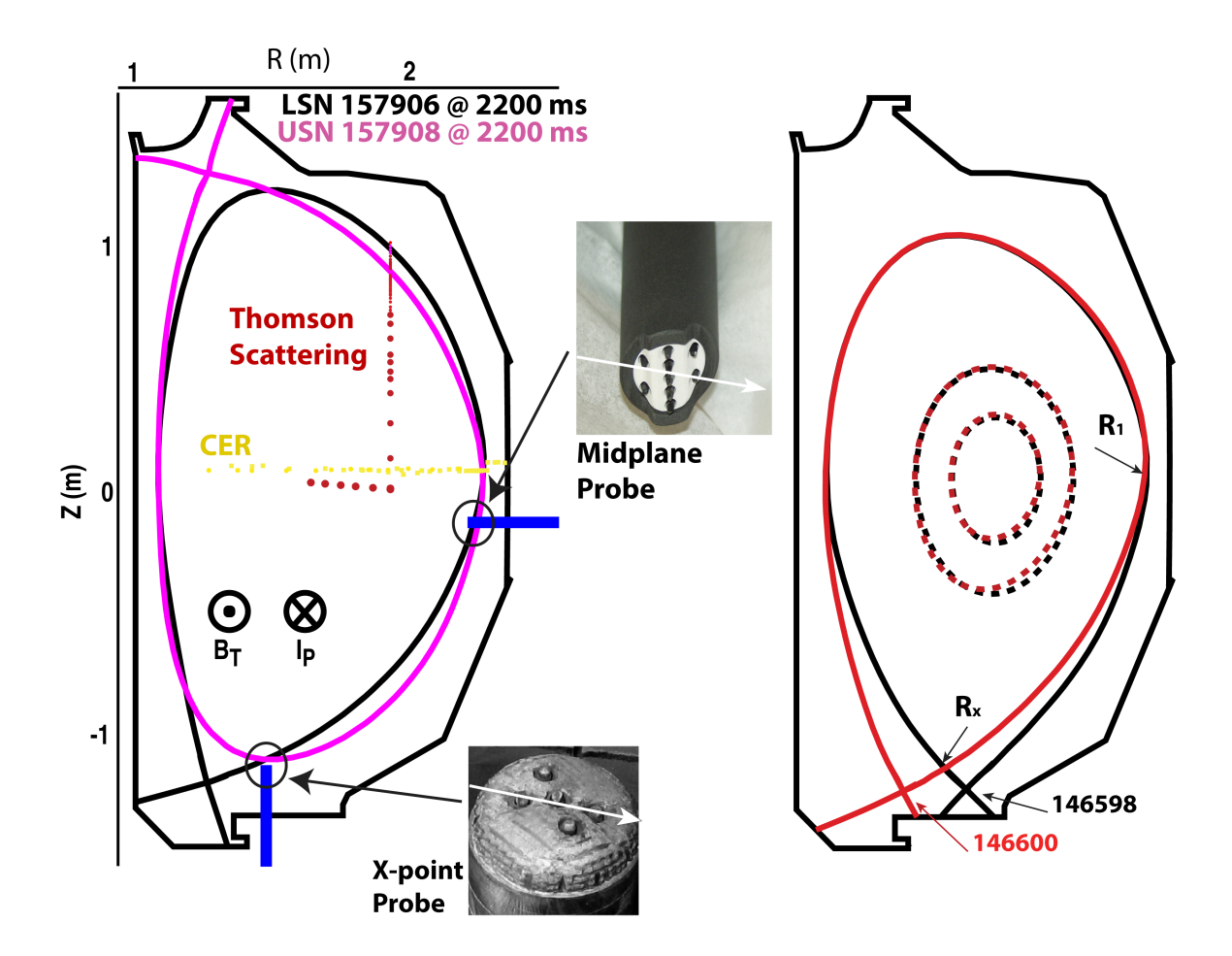


Fig. 2

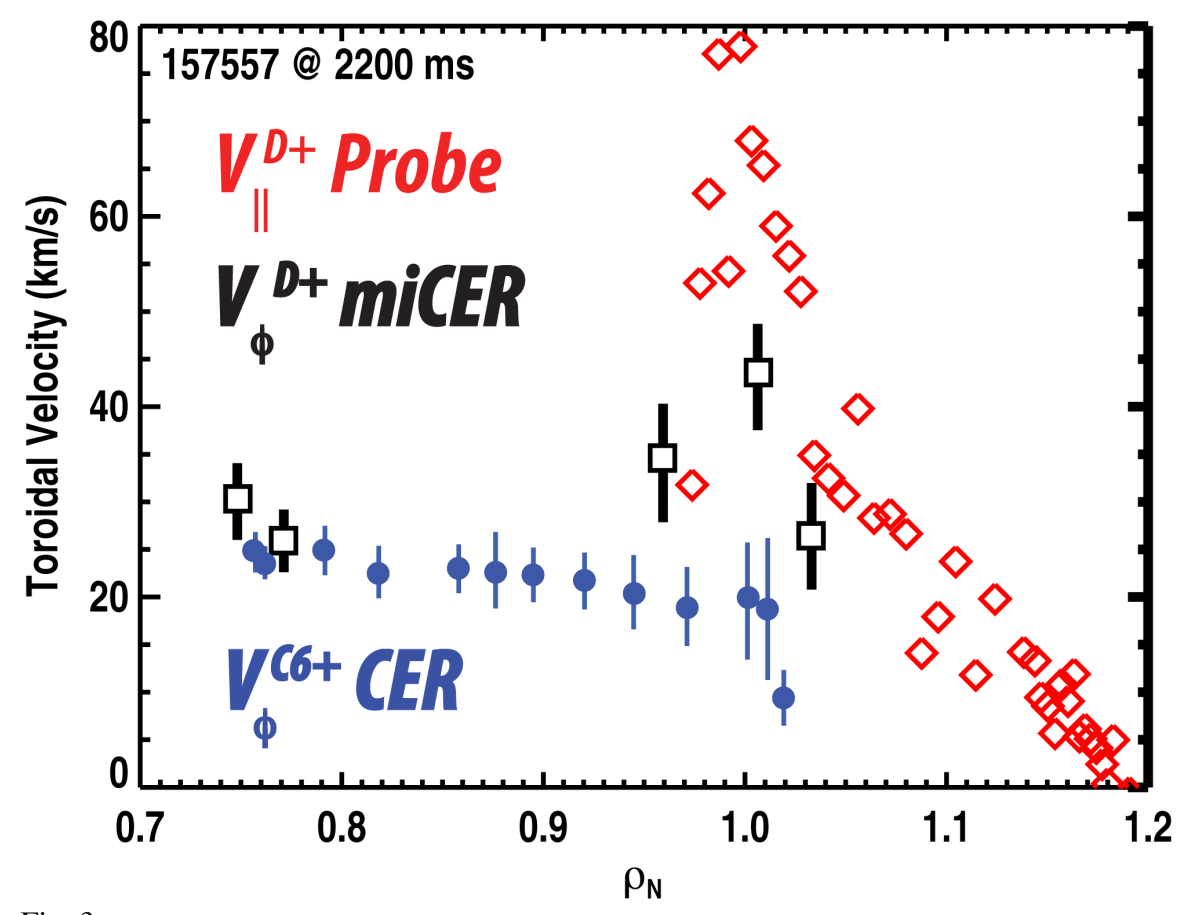


Fig. 3

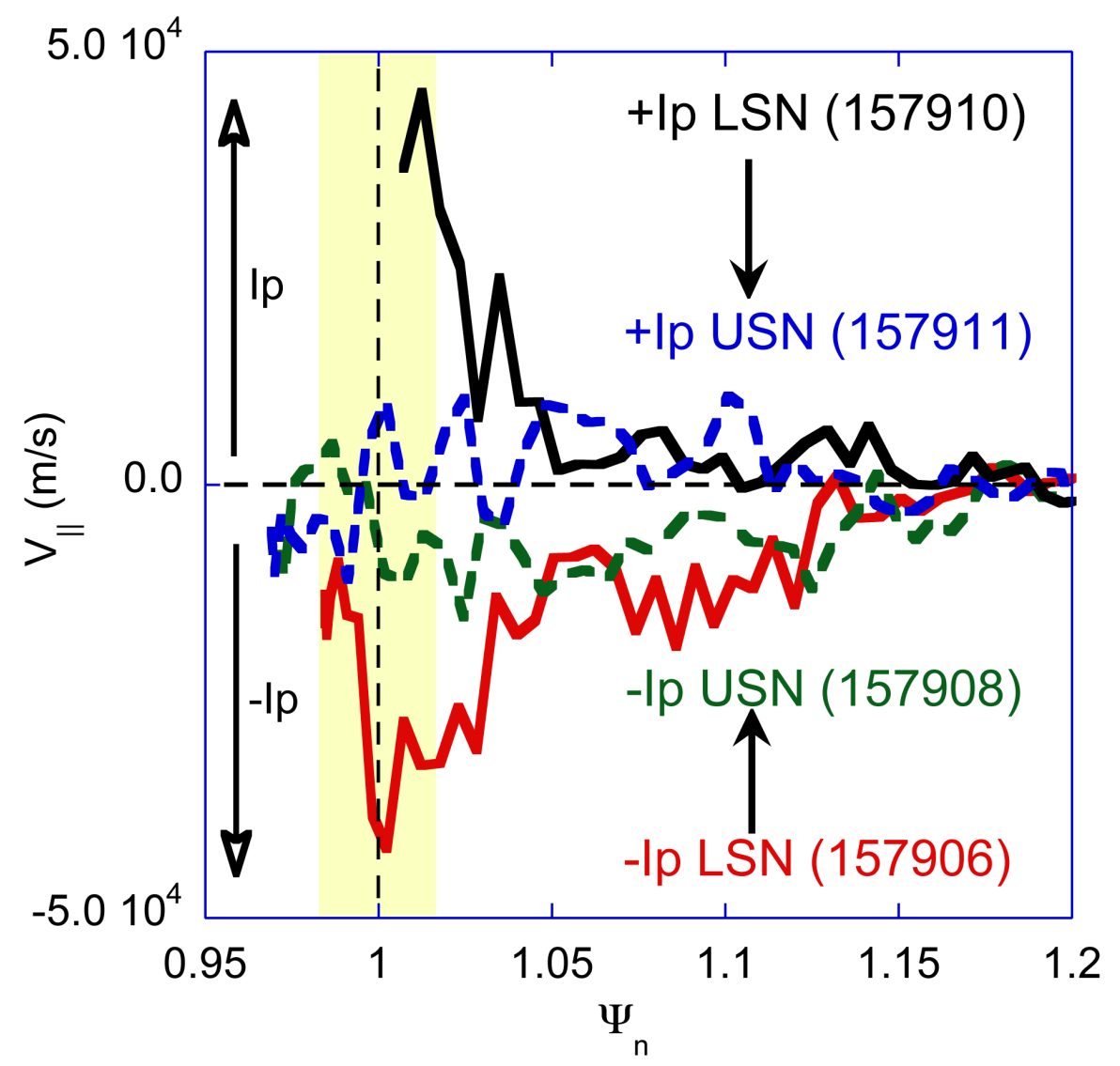


Fig. 4

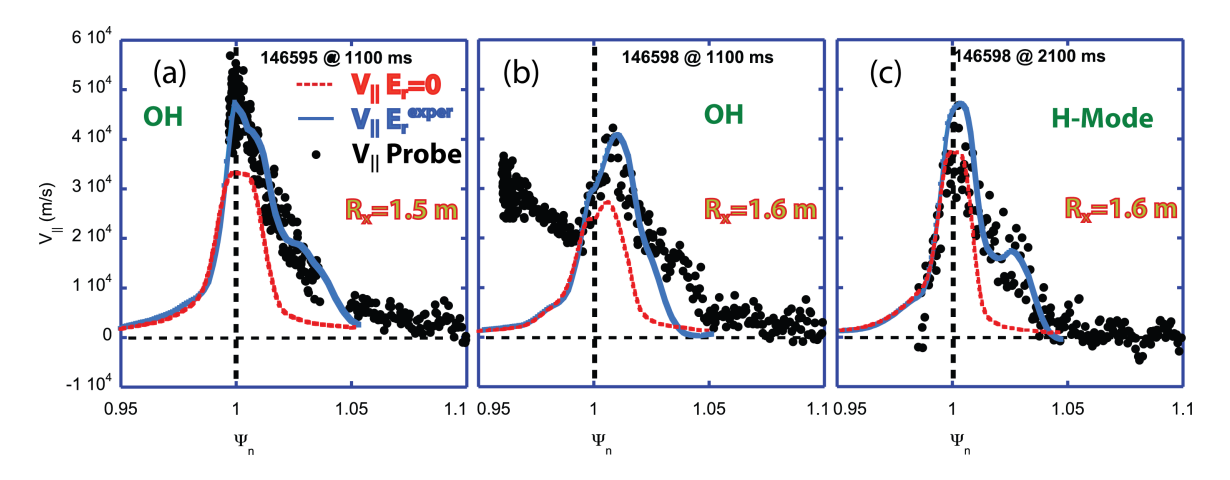


Fig. 5

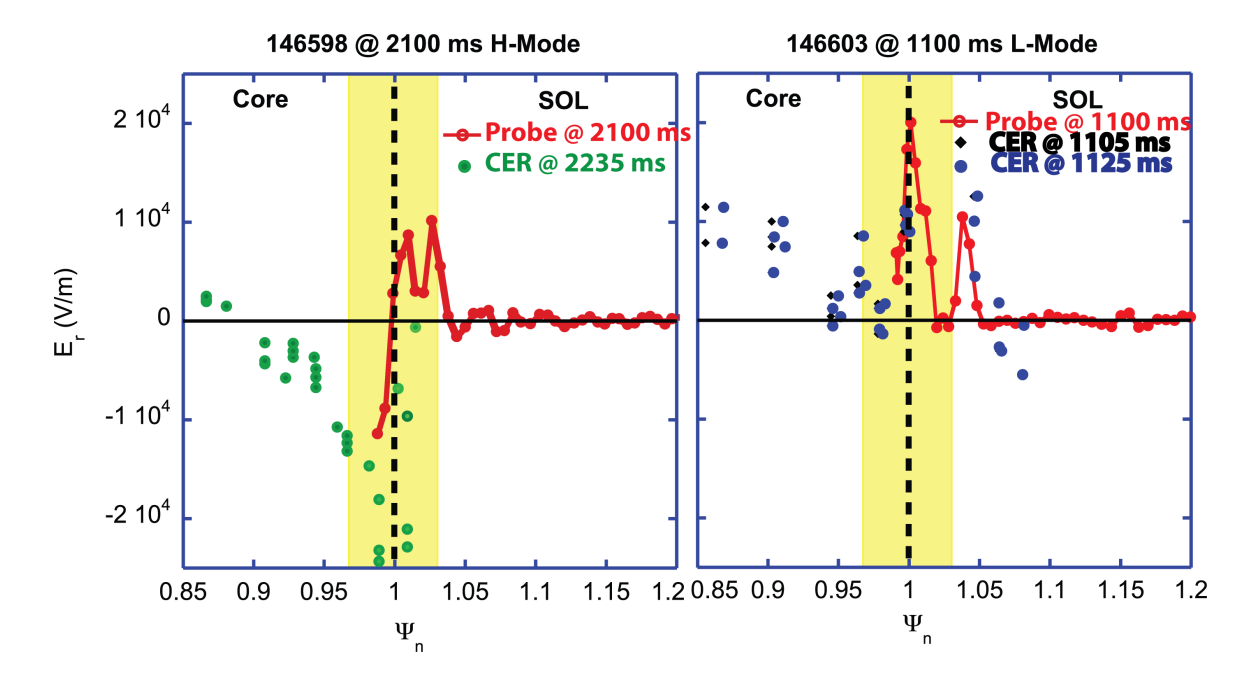


Fig. 6

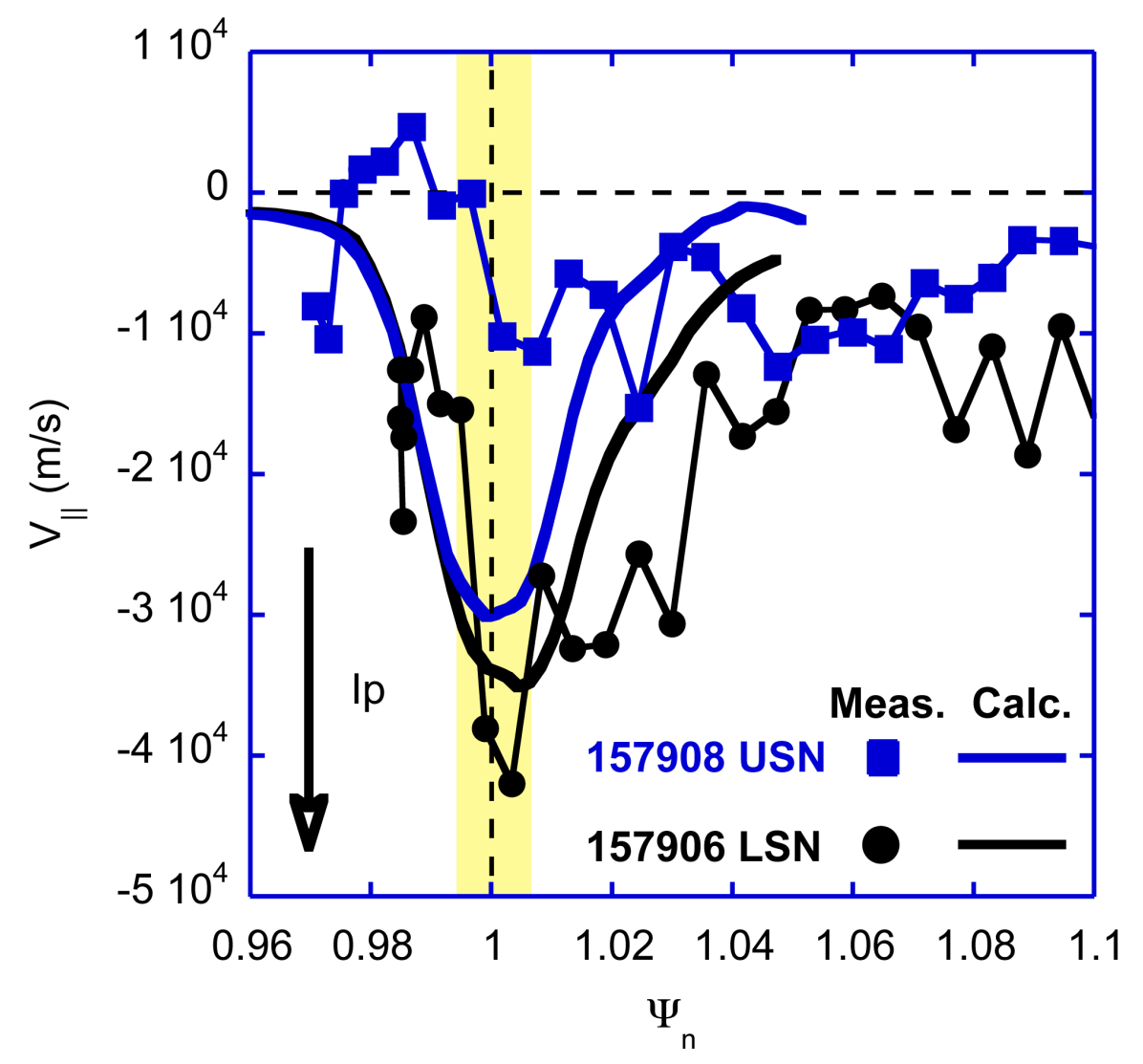


Fig. 7

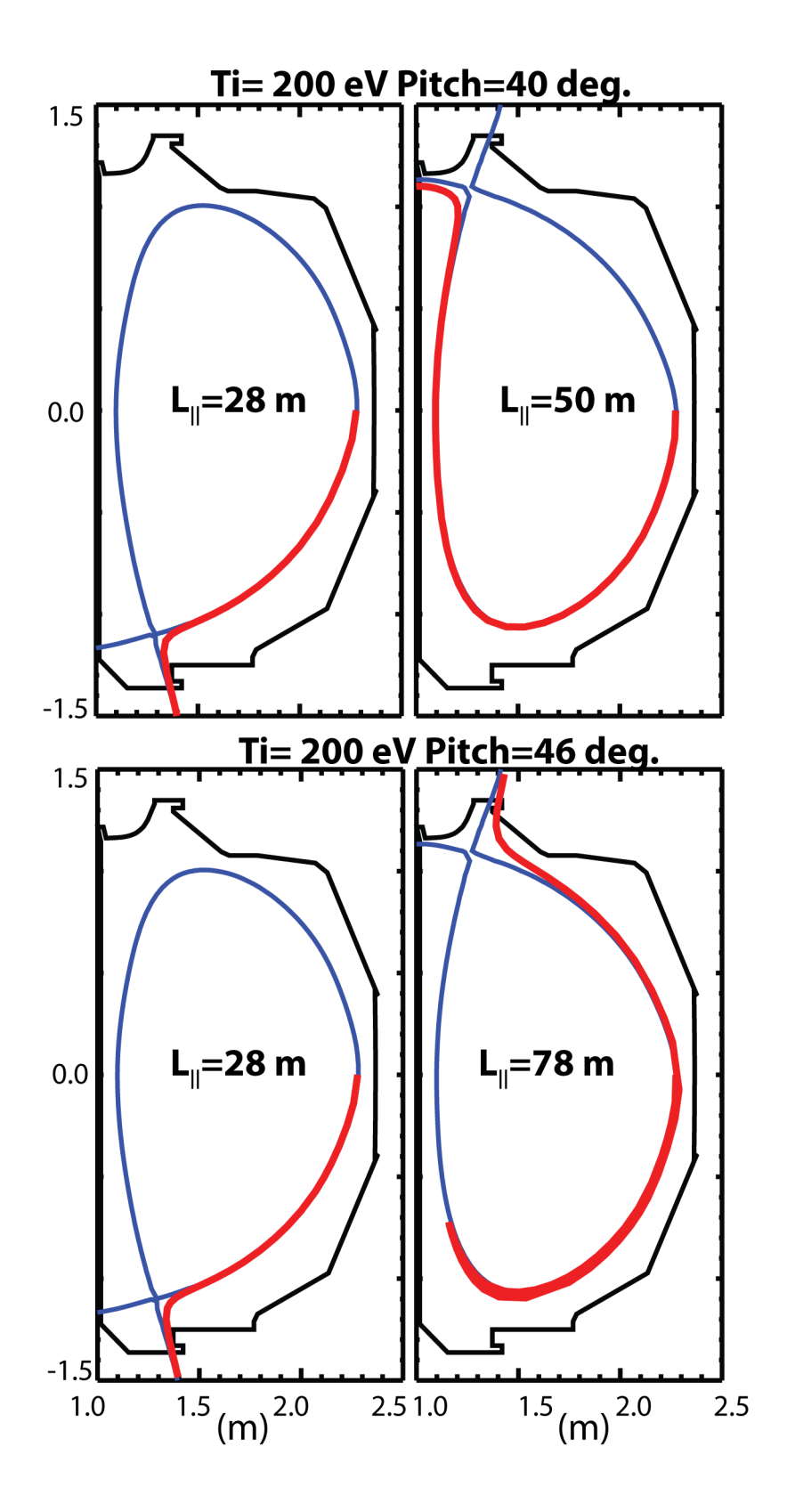


Fig. 8

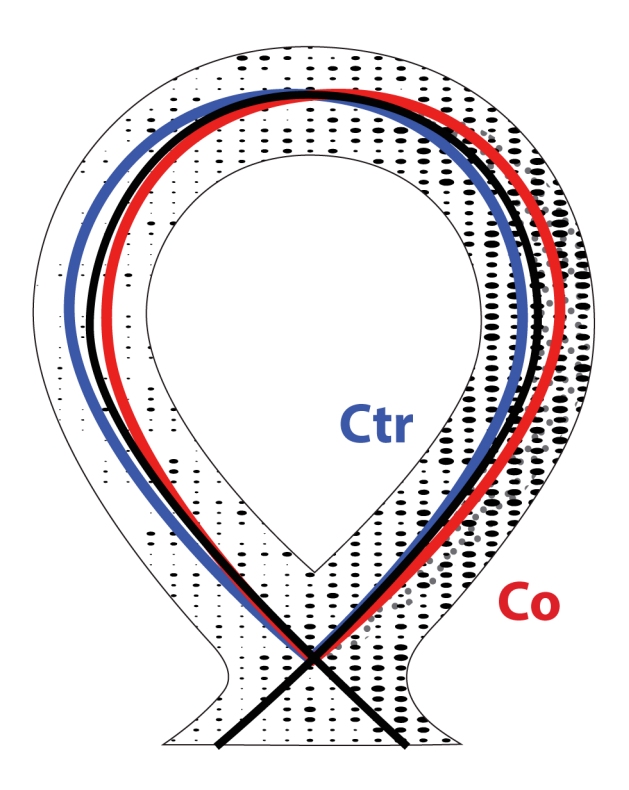


Fig. 9

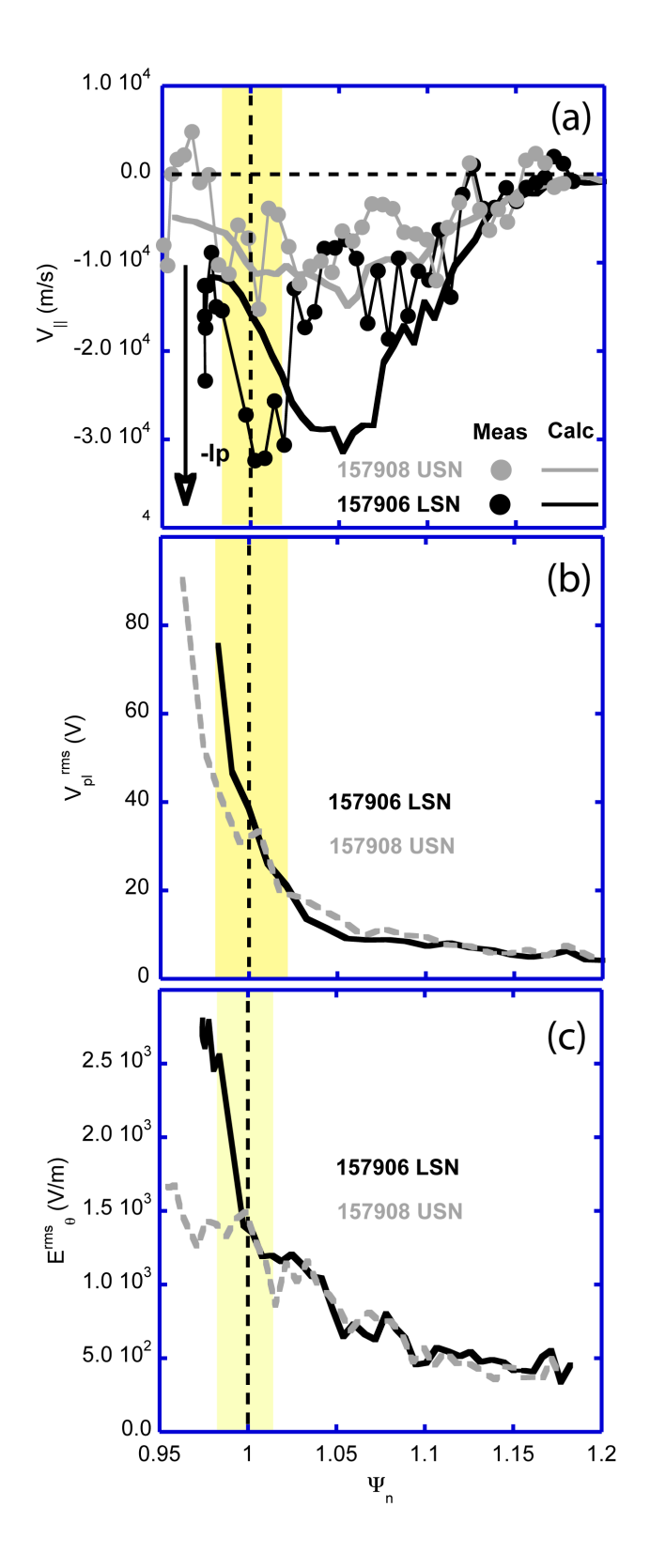


Fig. 10

## 159392 & 159394 @ 2230ms

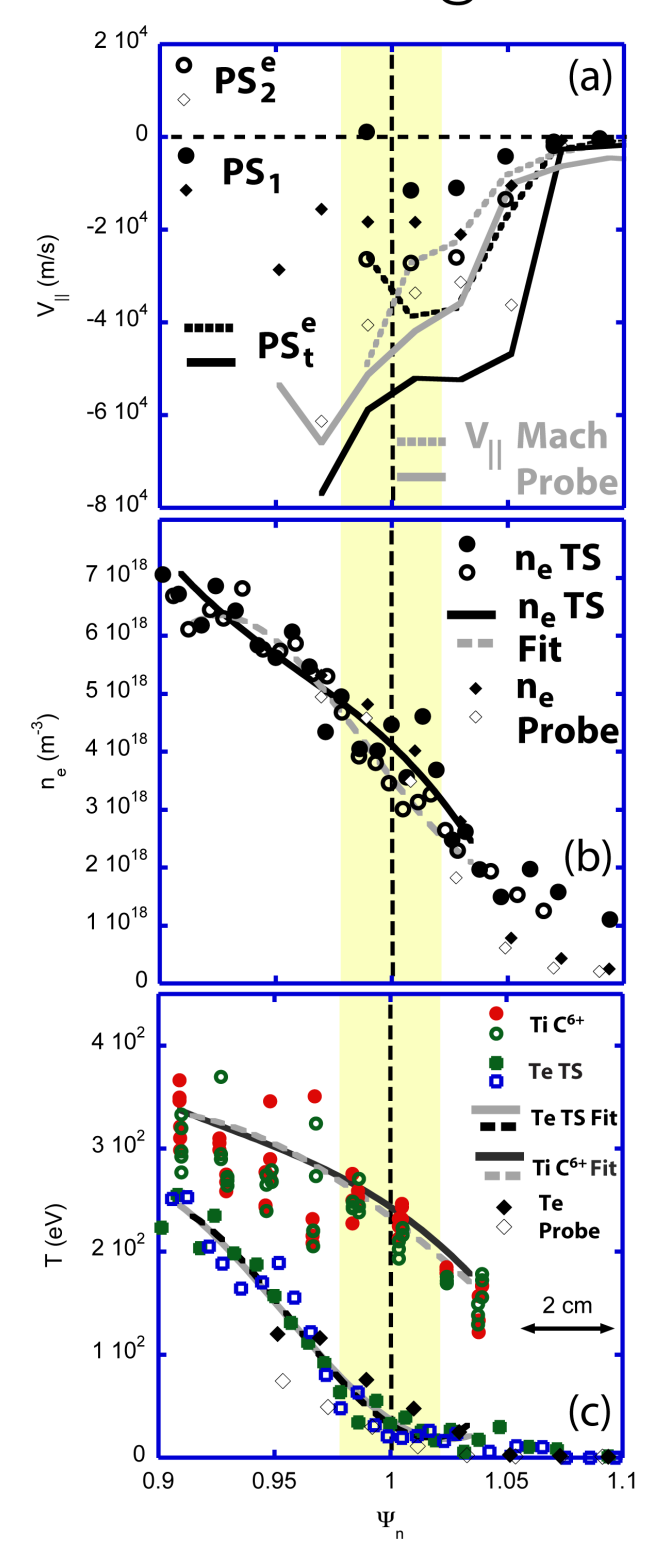


Fig. 11

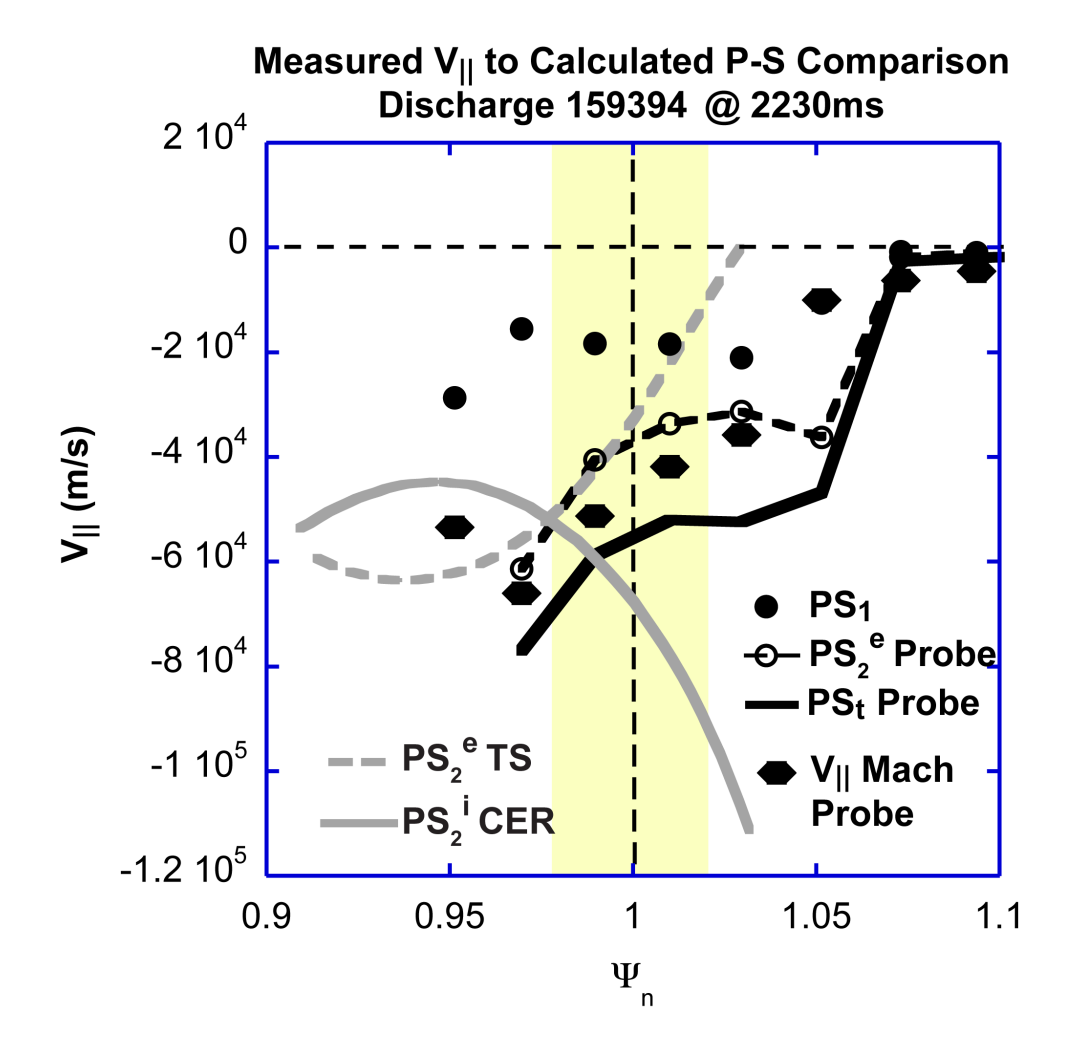


Fig. 12

## 157906 LSN vs 157908 USN 2 10<sup>4</sup> USN 0 -2 10<sup>4</sup> LSN -4 10<sup>4</sup> -6 10<sup>4</sup> $PS_{t}$ Probe V<sub>∥</sub> Mach Probe -8 10<sup>4</sup> -1 10<sup>5</sup> 1.05 1.15 0.95 1.1 1 1.2 $\Psi_{\text{n}}$

Fig. 13

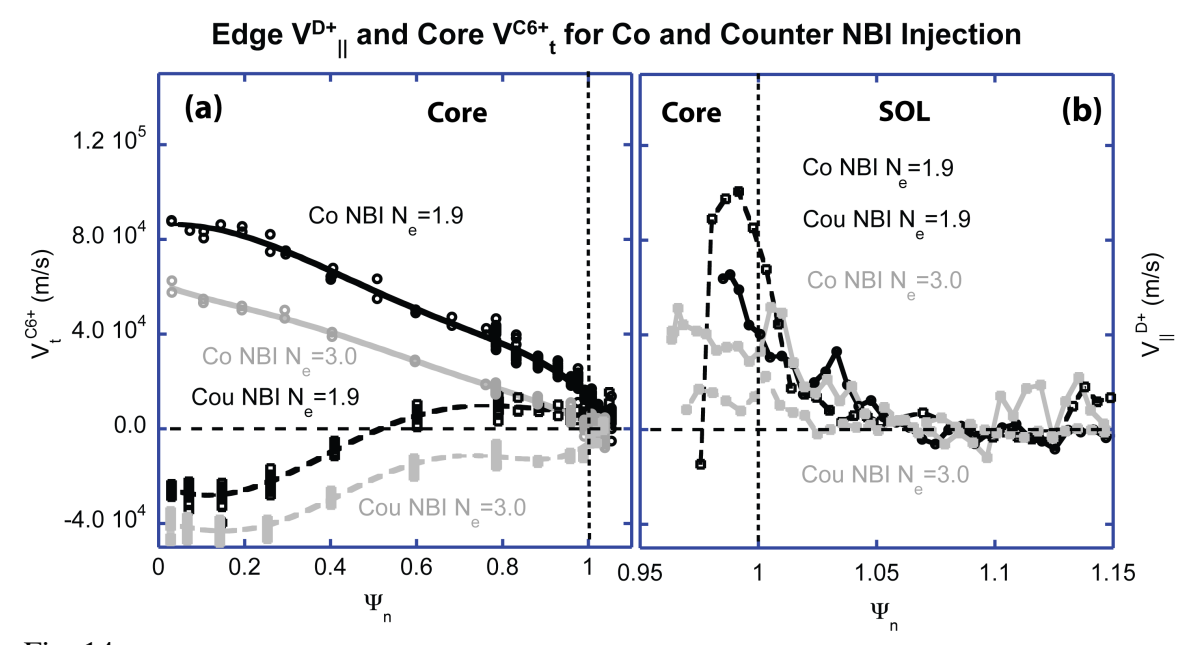


Fig. 14

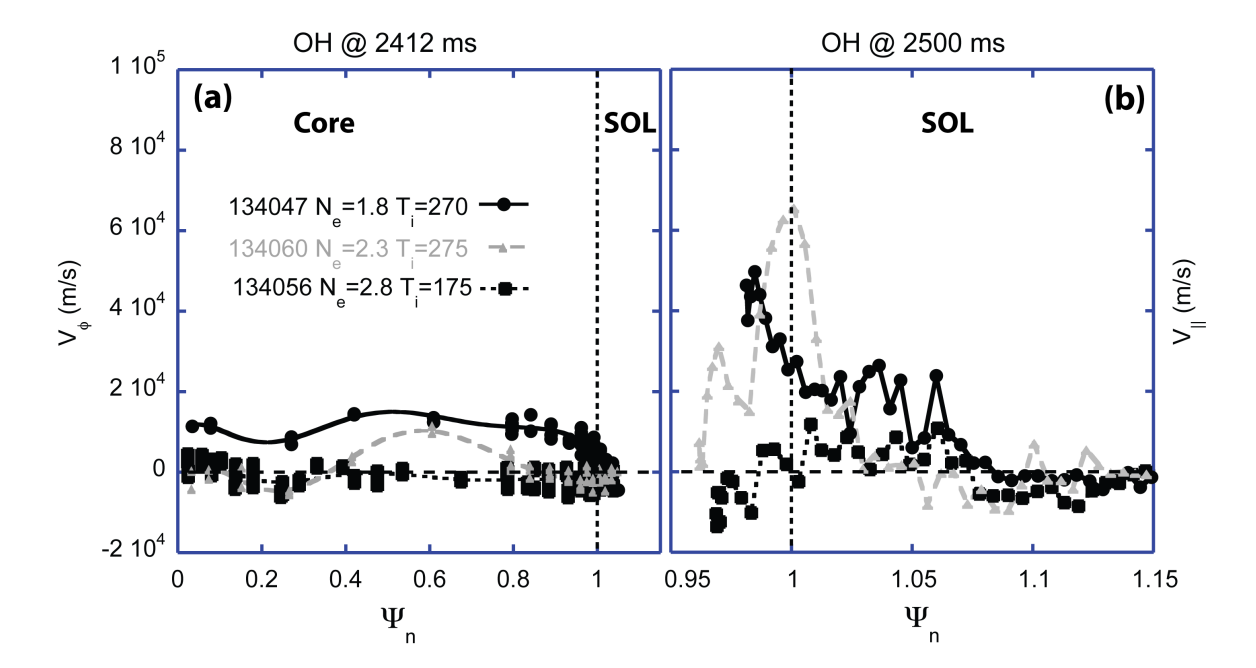


Fig. 15

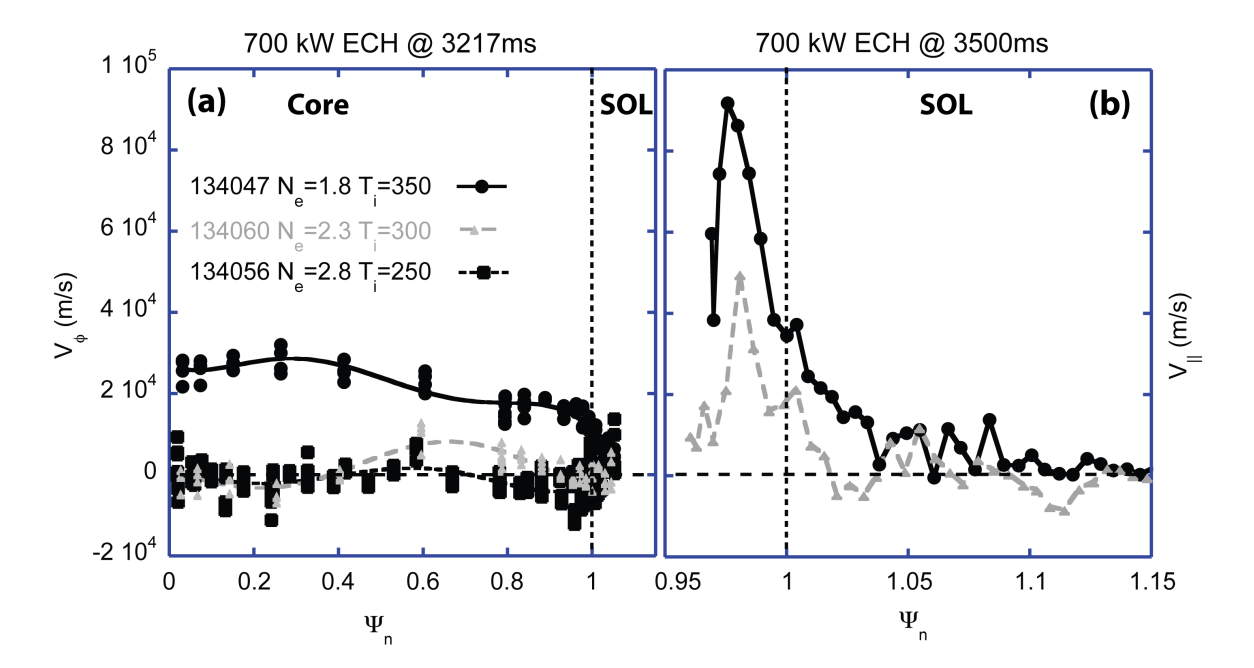


Fig. 16

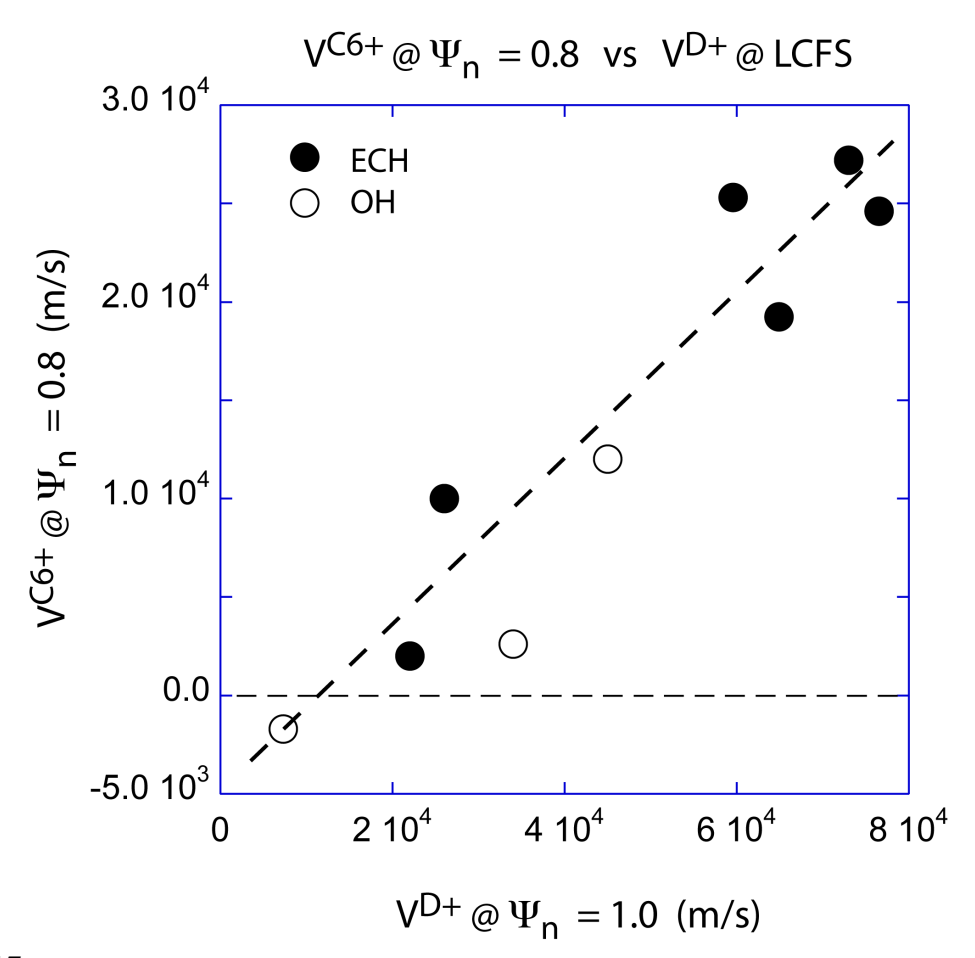


Fig. 17

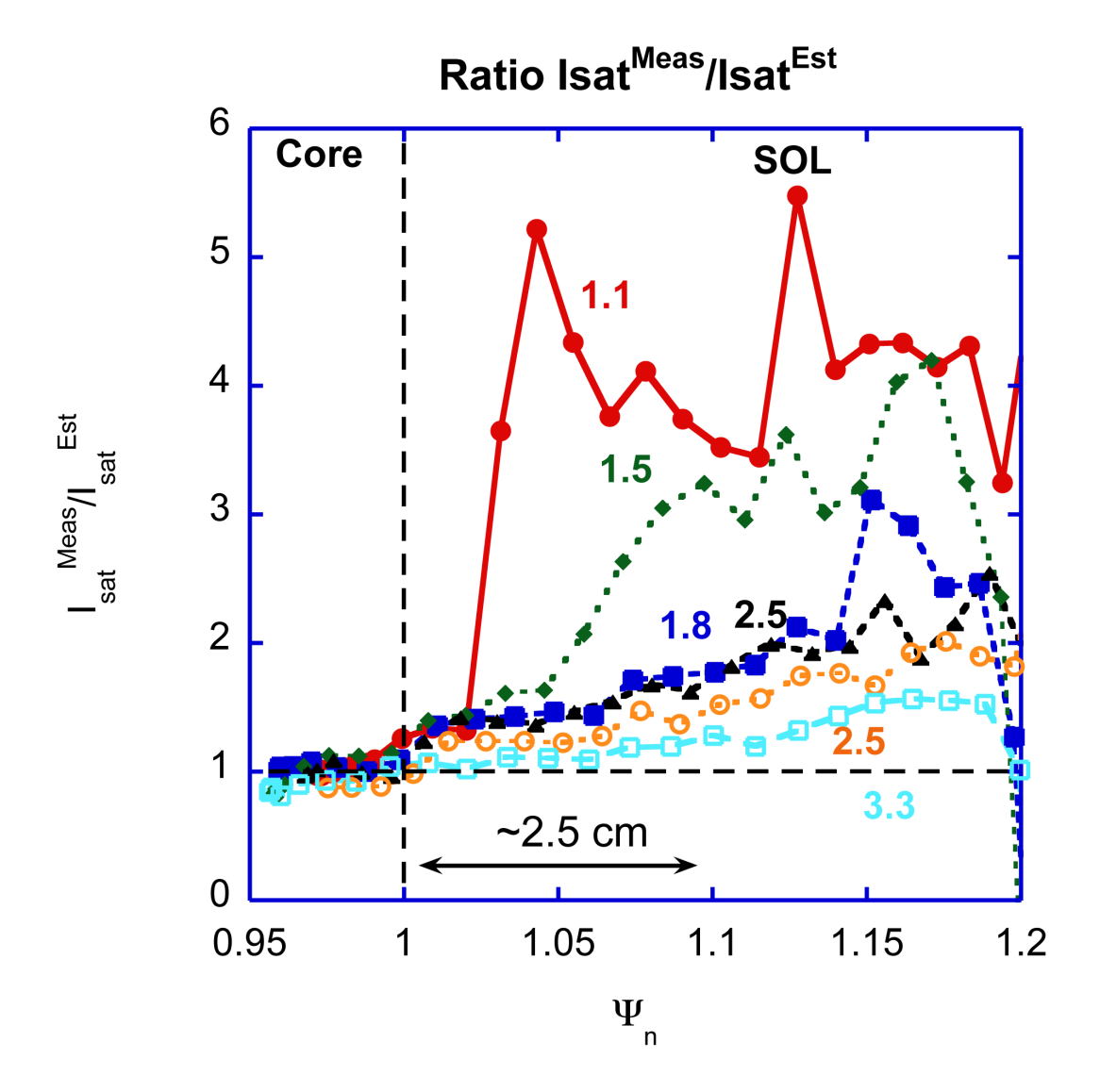


Fig. 18

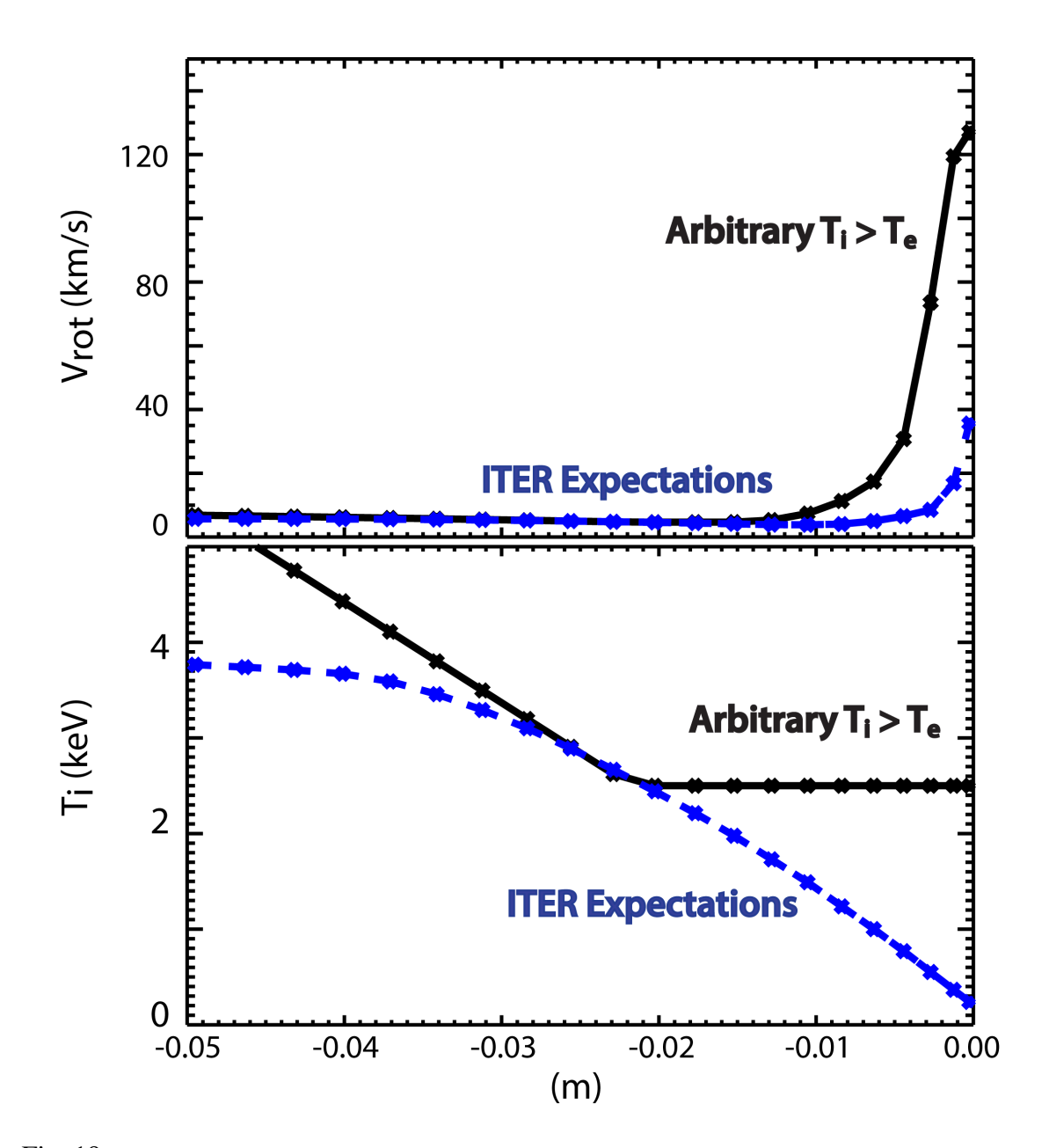


Fig. 19

<sup>1</sup> S. Suckewer, H. P. Eubank, R. J. Goldston, J. McEnerney, N. R. Sauthoff, H. H. Tower, Nuc. Fus., Vol. 21, No. 10 (1981) p1301.

<sup>2</sup> K. Ida, K. Kawahata, K. Toi, T. Watari, O. Kaneko, Y. Ogawa, H. Sanuki, K. Adati, R. Akiyama, A. Ando, R. Ando, Y. Hamada, *et al.* Nuc. Fus., Vol. 31, No. 5 (1991) p943

- <sup>3</sup> L. G. Eriksson, R. Gianella, T. Hellten, E. Kallne and G. Sundstrom, Plas. Phys. Cont. Fus. Vol. 34, No. 5 (1992) P 863
- <sup>4</sup> B. P. Duval, B. Joye, B. Marchal, Nuclear Fusion, Vol. 32, No. 8 (1992) p1405
- <sup>5</sup> L. G. Eriksson, E. Righi, K. D. Zastrow, Plas Phys Cont Fusion, 39 (1997) p27
- <sup>6</sup> J. E. Rice, M. Greenwald, I. H. Hutchinson, E. S. Marmar, Y. Takase, S. M. Wolfe, F. Bombarda, Nuclear Fusion, Vol. 38, No. 1 (1998) p75.
- <sup>7</sup> J. E. Rice, P. T. Bonoli, J. A. Goetz, M. J. Greenwald, I. H. Hutchinson, E. S. Marmar, M. Porkolab, S. M. Wolfe, S J. Wukitch, Nuc. Fus. Vol. 39, No. 9 (1999) p1175.
- <sup>8</sup> J.M. Noterdaeme, R. Budny, A. Cardinali, C. Castaldo, R. Cesario, F. Crisanty, J. deGrassie, D. A. D'Ippolito, F. Durodie, A. Ekedahl, A. Figueiredo, *et al.*, Nucl. Fusion, No 43, (2003) 274
- <sup>9</sup> J. S. deGrassie, K. H. Burrell, L. R. Bayor, W. Houlberg and J. Lohr, Phys. Plasmas, No. 11, (2004) 4323
- <sup>10</sup> A. Bortolon, B. P. Duval, A. Pochelon, and A. Scarabioso, Phys. Rev. Lett., No. 97, (2006) 235003
- <sup>11</sup> J. E. Rice, A. Ince-Cushman, J. S. deGrassie, L. G. Erikcoon, Y. Sakamoto, A. Scarabioso, A. Bortolon, K. H. Burrell, B. P. Duval, C. Fenzi-Bonizec, M. J. Greenwald, R. J. Groebner, *et al.*, *Nucl. Fusion*, 47 (2007) 1618
- <sup>12</sup> J. S. deGrassie, J. E. Rice, K. H. Burrell, R. J. Groebner and W. M. Solomon, *Phys. Plasmas* **14** (**2007**) 056115
- <sup>13</sup> Eriksson L. G., Hoang G.T. and Bergeaud V., *Nucl. Fusion* **41** (2001) 91
- <sup>14</sup> Hutchinson I. H., Rice J. E., Granetz R. S. and Snipes J. A., *Phys. Rev. Lett.* **84** (**2000**) 3330
- <sup>15</sup> B. P. Duval, A. Bortolon, A. Karpushov, R. A. Pitts, A. Pochelon, A. Scarabosio and the TCV Team, Plasma Phys. Contr. Fus., Vol. 49, (2007) B195-B209.
- <sup>16</sup> A. Pochelon, Plas. Phys. Cont. Fus. (2007)
- <sup>17</sup> K. H. Burrell, Science **281**, 1816 (1998).
- <sup>18</sup> P. A. Politzer, C.C. Petty, R. J. Jayakumar, T. C. Luce, M. R. Wade, J. C DeBoo, J. R. Ferron, P. Gohil, C. T. Holcomb, A. W. Hyatt, J. Kinsey, R. J. LaHaye, M. A. Makowski and T. W. Petrie., Nucl. Fusion **48**, (2008) 075001.
- <sup>19</sup> G.R. McKee, P. Gohil, D.J. Schlossberg, J.A. Boedo, K.H. Burrell, J.S. deGrassie, R.J. Groebner, R.A. Moyer, C.C. Petty, T.L. Rhodes, L. Schmitz, M.W. Shafer, W.M. Solomon, M. Umansky, G. Wang, A.E. White, and X. Xu, Nucl. Fusion 49, 115016 (2009).
- <sup>20</sup> R.J. Buttery, R.J. La Haye, P. Gohil, G.L. Jackson, H. Reimerdes, and E.J. Strait, Phys. Plasmas **15**, 056115 (2008).
- <sup>21</sup> F. Wagner, G. Becker, K. Behringer, D. Campbell, A. Eberhagen, W. Engelhardt, G. Fussmann, O. Gehre, J. Gernhardt, G.V. Gierke, G. Haas, M. Huang, F. Karger, M. Keilhacker, O. Klüber, M. Kornherr, K. Lackner, G. Lisitano, G.G. Lister, H.M. Mayer, D. Meisel, E.R. Müller, H. Murmann, H. Niedermeyer, W. Poschenrieder,

- H. Rapp, H. Röhr, F. Schneider, G. Siller, E. Speth, A. Stäbler, K.H. Steuer, G. Venus, O. Vollmer, and Z. Yü, Phys. Rev. Lett **49**, 1408 (1982).
- <sup>22</sup> B. P. Duval, A. Bortolon, A. Karpushov, R. A. Pitts, A. Pochelon, O. Sauter, A Scarabosio, G. Turri and the TCV Team, Phys of Plas., No. 15, (2008) 056113.
- <sup>23</sup> A. Scarabosio, Phys. of Plas. (2008)
  <sup>24</sup> K. Nagashima, Y. Koide and H. Shirai, Nuc. Fus., Vol. 34, No. 3, 449, (1994)
- <sup>25</sup> W.M. Solomon, S.M. Kaye, R.E. Bell, B.P. LeBlanc, J.E. Menard, G. Rewoldt, and W. Wang, Phys. Rev. Lett. 101, 065004 (2008).
- <sup>26</sup> B. Coppi, Plasma Phys. Control. Fusion **36** (1994) B107-B121.
- <sup>27</sup> B. Coppi, G. Penn, L. E. Sugiyama, Proceedings 17<sup>th</sup> International Fusion Energy Conference, IAEA-F1-CN-TH3/7 (1998).
- <sup>28</sup> B. Coppi, Proceedings 18<sup>th</sup> International Fusion Energy Conference, IAEA-CN-77/THP1/17 (2000).
- <sup>29</sup> J. S. deGrassie, R. J. Groebner, K. H. Burrell and W. M. Solomon, Nuc. Fus., **49** (2009) 085020
- <sup>30</sup> J.S. deGrassie, S. H. Mueller and J. A. Boedo, Nucl. Fusion **52**, 013010 (2012).
- <sup>31</sup> W. M. Stacey, J. A. Boedo, T. E. Evans, B. A. Grierson, and R. J. Groebner, Phys of Plas. **19**, 112503 (2012)
- <sup>32</sup> K. C. Shaing, Phys. Plasmas, **8** 193 (2001)
- <sup>33</sup> B. Coppi, Nuc. Fusion, **42**, 1 (2002).
- <sup>34</sup> P. H. Diamond, C. J. McDevitt, O. D. Gurcan, T. S. Hahm and V. Naulin. Phys. Plasmas **14** 122507 (2007)
- <sup>35</sup> R.R. Dominguez and G.M. Staebler, Phys. Fluids **B** 5, 3876 (1993)
- <sup>36</sup> O.D. Gurcan, P.H. Diamond, T.S. Hahm, and R. Singh, Phys. Plasma 14, 042306 (2007).
- <sup>37</sup> T. Stoltzfus-Dueck, Phys. of Plas., No. 19, (2012) 055908.
- <sup>38</sup> T. Stoltzfus-Dueck, Phys. Rev. Lett., 108, (2012), 065002.
- <sup>39</sup> P.H. Diamond, C.J. McDevitt, Ö.D. Gürcan, T.S. Hahm, and V. Naulin, Phys. Plasmas **15**, 012303 (2008).
- <sup>40</sup> G.R. Tynan, P.H. Diamond, C. Holland, S.H. Muller, M. Xu, Z. Yan, and J. Yu, Plasma Phys. Control. Fusion **51**, 124055 (2009).
- <sup>41</sup> N. Smick, B. LaBombard, C.S. Pitcher, J. Nucl. Mater. **337-339**, 281-285 (2005).
- <sup>42</sup> B. LaBombard, J.E. Rice, A.E. Hubbard, J.W. Hughes, M. Greenwald, J. Irby, Y. Lin, B. Lipschultz, E.S. Marmar, C.S. Pitcher, N. Smick, S.M. Wolfe, S.J. Wukitch, and the Alcator Group, Nucl. Fusion 44, 1047-1066 (2004).
- <sup>43</sup> A. Loarte, R. Pitts, A. Polevoi, private communication (2014).
- <sup>44</sup> Y. Martin, T. Takizuka, and ITPA CDBM H-mode Database Working Group. Journal of Physics, 123 (2008) 012033
- <sup>45</sup> Z. Yan, G. R. McKee, J.A. Boedo, D. L. Rudakov, L. Schmitz, P. H. Diamond, G. Tynan, R. J. Fonck, R. J. Groebner, T. H. Osborne and P. Gohil. Nuc. Fusion, 52 (2013) 113038.
- <sup>46</sup> J.C. Luxon, L.G. Davis, Fusion Technology **8**, Part 2A, 441 (1985).
- <sup>47</sup> T. N. Carlstrom, G. L. Campbell, J. C. DeBoo, R. Evanko, J. Evans, C. M Greenfield, J. Haskovec, C. L. Hsieh, E. McKee, R. T. Snider, et al. Rev. Sci. Instrum., Vol. 63. (1992), p 4901

- <sup>48</sup> B. A. Grierson, K. H. Burrell, W. M. Solomon and N. A. Pablant, Rev. Sci. Inst., No 81, (2010), 10D735
- <sup>49</sup> B. A. Grierson, K. H. Burrell, W. W. Heidbrink, M. J. Lanctot, N. A. Pablant and W. M. Solomon, Phys. Plas., no. 19, (2012), 056107
- J. A. Boedo, E. A. Belli, E. Hollmann, W. H. Solomon, D. Rudakov, J. G. Watkins, R. Prater, J. Candy, R. J. Groebner, K. H. Burrell, J. S. deGrassie, *et al.* Phys. Plas., Vol. 18, No 3 (2011), p. 032510
- <sup>51</sup> S. H. Muller, J. A. Boedo, K. H. Burrell, J. S. DeGrassie, R. A. Moyer, D. L. Rudakov, W. M. Solomon and G. R. Tynan, Phys. Plas, Vol. 18, (2011), p 072504
- <sup>52</sup> A. V. Chankin and G. M. McCracken, Nuc. Fus., Vol. 33 (10), (1993), p. 1459.
- <sup>53</sup> C. S. Chang and S. Ku, Phys. Plas., Vol. 15, (2008), p. 062510
- <sup>54</sup> K. C. Shaing, Phys. of Plas., Vol. 9, No. 1, (2002)
- <sup>55</sup> D. M. Thomas, A. W. Leonard, T. H. Osborne, R. J. Groebner, W. P. West and K. H Burrell. Plasma Phys. Control. Fusion 48, (2006), A183-A191
- <sup>56</sup> T. S. Hahm, Phys. Fluids., 31, (1988), 2670.
- <sup>57</sup> J. Hugill, JNM, 196-198 (1992), 918-922.
- A. Chankin, D. Coster, N. Asakura, G. Corrigan, S. K. Erents, W. Fundamenski, H. W. Muller, R. A Pitts, P. C. Stangeby, M. Wischmeier, Nucl. Fusion, 47 (2007) 762-772
   B. LaBombard, S. Gangadhara, B. Lipschultz, C. S. Pitcher. J. Nuc. Mater. 313-316 (2003) 995.
- <sup>60</sup> R. A. Pitts, J. Horacek, W. Fundamenski, O. E. Garcia, A. H. Nielsen, M. Wischmeier, V. Naulin, J. Juul Rasmussen, J. Nuc. Mater., 3630365, (2007) 505-510.
- <sup>61</sup> K. Hoshino, A. Hatayama, N. Asakura, H. Kawashima, R. Schneider, D. Coster, J. Nuc. Mater., 363-365, (2007) 539-543.
- <sup>62</sup> D. J. Battaglia, K. H. Burrell, C. S. Chang, S. Ku, J. S. deGrassie, and B. Grierson, Phys. Plas., No. 21, (2014) 072508.
- <sup>63</sup> J. E. Rice, B. P. Duval, M. L. Reinke, Y. A. Podpaly, A. Bortolon, R. M. Churchill, J. Cziegler, P. H. Diamond, A. Dominguez, P. C. Ennever, C. L. Fiore, *et al*, Nuc. Fus., Vol. 51, (2011) 083005
- <sup>64</sup> A. E. White, N. T. Howard, M. Greenwald, M. Reinke, C. Sung, S. Baek, M. Barnes, J. Candy, A. Dominguez, D. Ernst, C. Gao, *et al.* Phys of Plas., No 20, (2013), 056106
- <sup>65</sup> A. Bortolon, B. P. Duval, A. Pochelon, A. Scarabioso, Phys. Rev. Lett., No. 97, (2006) 235003
- <sup>66</sup> M. Barnes, F. I Parra, J. P. Lee, E. A. Belli, M. F. F. Nave and A. E. White, Phys. Rev. Lett., Vol. 111, (2013) 055005
- <sup>67</sup> I. Langmuir and H. Mott-Smith, Phys Rev., No 28, (1926) 727-763.
- 68 N. Hershkowitz, "Plasma Diagnostics, Discharge Parameter and Chemistry", Ed. O. Auciello and D. L. Flamm (Academic, Boton, 1989), Vol. 1, Chap. 3.
- <sup>69</sup> J. A. Boedo, D. Gray, R. W. Conn, P. Luong, M. Schaffer, R. S. Ivanov, A. V. Chernilevsky, G. Van Oost, Rev. Sci. Inst., Vol. 70, No 7, (1999), p 2997
- <sup>70</sup> D. L. Rudakov, J. A. Boedo, R. A. Moyer, R. D. Lehmer and G. Gunner, Rev. Sci. Inst., Vol. 72, No. 1 (2001) 453
- <sup>71</sup> A. R. Polevoi, S. Y., Medvedev, V. s. Mukhovatov, A. S. Kukushkin, Y. Murakami, M. Shimada and A. Ivanov, J. Plasma Fusion Res. Series, Vol. 5, (2002) 82-87

<sup>72</sup> A. R. Polevoi, R. Pitts, private communication (2014)